Magmatic Evolution and Ascent History of the Aries Micaceous Kimberlite, Central Kimberley Basin, Western Australia: Evidence from Zoned Phlogopite Phenocrysts, and UV Laser $^{40}Ar/^{39}Ar$ Analysis of Phlogopite–Biotite

PETER J. DOWNES[1]*, JO-ANNE WARTHO[2] AND BRENDAN J. GRIFFIN[3]

[1]WESTERN AUSTRALIAN MUSEUM, FRANCIS ST, PERTH, WESTERN AUSTRALIA, 6000, AUSTRALIA

[2]JOHN DE LAETER CENTRE OF MASS SPECTROMETRY, DEPARTMENT OF APPLIED GEOLOGY, CURTIN UNIVERSITY OF TECHNOLOGY, HAYMAN ROAD, BENTLEY, WESTERN AUSTRALIA, 6102, AUSTRALIA

[3]CENTRE FOR MICROSCOPY AND MICROANALYSIS, UNIVERSITY OF WESTERN AUSTRALIA, CRAWLEY, WESTERN AUSTRALIA, 6009, AUSTRALIA

The Neoproterozoic Aries kimberlite was emplaced in the central Kimberley Basin, Western Australia, as a N–NNE-trending series of three diatremes infilled by lithic-rich kimberlite breccias. The breccias are intruded by hypabyssal macrocrystic phlogopite kimberlite dykes that exhibit differentiation to a minor, high-Na–Si, olivine–phlogopite–richterite kimberlite, and late-stage macrocrystic serpentine–diopside ultramafic dykes. Mineralogical and geochemical evidence suggests that the high-Na–Si, olivine–phlogopite–richterite kimberlite was derived from the macrocrystic phlogopite kimberlite as a residual liquid following extended phlogopite crystallization and the assimilation of country rock sandstone, and that the macrocrystic serpentine–diopside ultramafic dykes formed as mafic cumulates from a macrocrystic phlogopite kimberlite. Chemical zonation of phlogopite–biotite phenocrysts indicates a complex magmatic history for the Aries kimberlite, with the early inheritance of a range of high-Ti phlogopite–biotite xenocrysts from metasomatized mantle lithologies, followed by the crystallization of a population of high-Cr phlogopite phenocrysts within the spinel facies lithospheric mantle. A further one to two phlogopite–biotite overgrowth rims of distinct composition formed on the phlogopite phenocrysts at higher levels during ascent to the surface. Ultra-violet laser $^{40}Ar/^{39}Ar$ dating of mica grain rims yielded a kimberlite eruption age of $815\cdot4 \pm 4\cdot3$ Ma (95% confidence). $^{40}Ar/^{39}Ar$ laser profiling of one high-Ti phlogopite-biotite macrocryst revealed a radiogenic ^{40}Ar diffusive loss profile, from which a kimberlite magma ascent duration from the spinel facies lithospheric mantle was estimated (assuming an average kimberlite magma temperature of $1000°C$), yielding a value of $\sim 0\cdot23$–$2\cdot32$ days for the north extension lobe of the Aries kimberlite.

INTRODUCTION

The Kimberley region of northern Western Australia preserves an extended record of alkaline mafic to ultramafic magmatism dating from Mesoproterozoic to Tertiary times (Jaques et al., 1986). Kimberlites, lamproites, ultramafic lamprophyres and carbonatites

*Corresponding author. Telephone: 61 8 94272735. Fax: 61 8 94272882. E-mail: peter.downes@museum.wa.gov.au

intrude the Kimberley Craton, and the surrounding Proterozoic King Leopold and Halls Creek Orogens (Fig. 1). Apart from the eruption of the Argyle lamproite at 1178 ± 47 Ma (Rb–Sr; Pidgeon et al., 1989), alkaline magmatism in the region falls into two major episodes: (1) an ~800 Ma event that produced the North Kimberley Province kimberlites, kimberlites and ultramafic lamprophyres in the East Kimberley Province, and the Aries kimberlite in the Central Kimberley (Edwards et al., 1992); (2) a ~22–18 Ma phase that produced the extensive West Kimberley lamproite field (Jaques et al., 1986) and lamproites in the Bonaparte Gulf (Gorter & Glikson, 2002).

The Aries micaceous kimberlite was emplaced during the Neoproterozoic phase of alkaline magmatism and has been previously dated at 820 ± 20 Ma (Rb–Sr on a mica separate from diamond drill-hole PRBH 45 in the north extension lobe; Smith, 1989). It has close mineralogical affinities to Group 2 kimberlites (orangeites) and olivine lamproites, but exhibits distinctive geochemical characteristics, notably the Nd–Sr isotopic signature of a Group 1 kimberlite (Edwards et al., 1992; Taylor et al., 1994). Initial studies of the Aries kimberlite included descriptions of its mineralogy, petrology and geochemistry (Edwards, 1990; Edwards et al., 1992), exploration history and evaluation (Towie et al., 1994) and indicator mineral chemistry (Ramsay et al., 1994). Since that time, an improved understanding of the geology of the Aries kimberlite has been made possible through further sampling of each of the kimberlite lobes by diamond drilling, which has produced over 7000 m of drill-core material that extends to a maximum depth of >300 m. There is, thus, a more extensive collection of material compared to the previous eight drill-cores that only penetrated to ≤100 m (Edwards et al., 1992), which forms the basis of this study.

Throughout this paper, the terms 'macrocryst', 'phenocryst' and 'xenocryst' are used, respectively, to refer to crystals of uncertain, cognate and foreign origin to their host.

One of the interesting features of the phlogopite-rich, hypabyssal phases of the Aries kimberlite is the presence of phlogopite phenocrysts with complex chemical zonation involving up to four stages of growth (Edwards et al., 1992). Such compositional zonation in phenocrysts has provided important insights into magma evolution for a range of different magma compositions, ranging from rhyodacite to basalt (e.g. Pearce et al., 1987; Singer et al., 1993, 1995; Nakagawa et al., 2002), phonolites and minettes (O'Brien et al., 1988), lamproites (Toscani et al., 1995) and micaceous kimberlites (Hunter et al., 1984; Neal & Taylor, 1989; Wiese et al., 1996). Studies of this type for micaceous kimberlite magmas are relatively rare, probably because kimberlites that preserve such a complex record of phlogopite growth are themselves rare. Thus, the availability of new samples from the hypabyssal phases of the Aries kimberlite allows a more detailed examination of this phenocryst zonation in relation to magma evolution.

Among the new phlogopite–biotite parageneses in the hypabyssal phases of the Aries kimberlite that are recognized here, we describe high-Ti phlogopite–biotite macrocrysts that are commonly overgrown by later generations of phlogopite and may form the cores of some phlogopite phenocrysts. These macrocrysts are similar in texture and composition to aluminous biotite macrocrysts from Group 2 kimberlites (orangeites), and other micaceous kimberlites from South Africa, the USA and Canada ('type 1' micas of Smith et al., 1978; Hall et al., 1989; Mitchell & Meyer, 1989; Mitchell, 1995; Wiese et al., 1996). The origin of these aluminous biotite macrocrysts is uncertain, but they may have been derived from mixing with other mantle-derived magmas or through inheritance from mantle or crustal lithologies (Smith et al., 1978; Mitchell, 1995). Mitchell (1995) suggested that the macrocrysts were distinctive of Group 2 kimberlite (orangeite) magmas, or their source regions in the Kaapvaal Craton. In our study, we test these hypotheses by examining a possible link between the Aries macrocrysts and high-Ti phlogopite–biotite in associated metasomatized ultramafic xenoliths.

An estimate of ascent duration for the Aries kimberlite magma has been obtained by high spatial resolution ultra-violet (UV) laser ^{40}Ar/^{39}Ar analysis of a radiogenic ^{40}Ar (^{40}Ar*) diffusive loss profile in one of these high-Ti phlogopite–biotite macrocrysts. By integrating the paragenesis of the high-Ti phlogopite–biotite macrocrysts into the crystallization history of the magma, as recorded in the various phlogopite growth zones, combined with the estimate of the duration of ascent, it is possible to track the ascent path of the Aries kimberlite magma. Determining the ascent history of a kimberlite magma from its depth of origin to the surface is a task that is rarely achieved, but may have implications for the preservation of diamonds in the kimberlite (cf. Franz et al., 1996; Pearson et al., 1997; Canil & Fedortchouk, 1999; Wartho & Kelley, 2003).

GEOLOGICAL SETTING

The Kimberley Craton is covered by an extensive Palaeoproterozoic sedimentary sequence that comprises the Kimberley and Speewah Basins (Fig. 1). The basement to the Kimberley and Speewah Basins generally is not exposed at the surface; however, geophysical and geochronological data suggest that the shallow basement comprises a late Archaean to early Proterozoic granitic terrain that is composed of NE-trending magmatic arcs and continental fragments (Gunn & Meixner, 1998; Tyler et al., 1999). This terrain
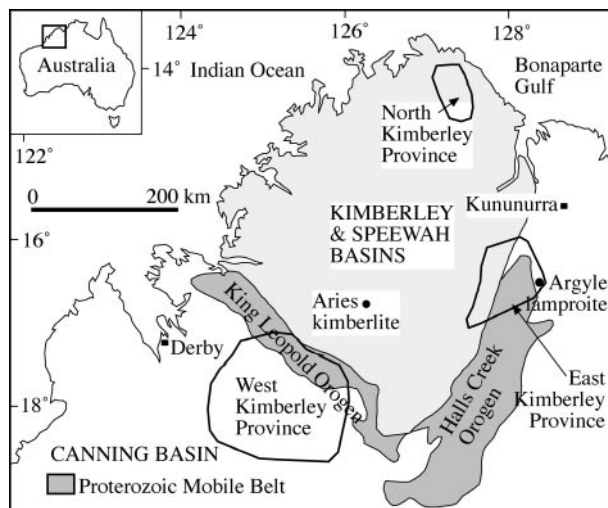
Fig. 1. Map showing the location of the Aries kimberlite and the North, East and West Kimberley kimberlite–lamproite provinces in the Kimberley region of Western Australia. The outline of the Kimberley and Speewah Basins is approximately the same as that of the Kimberley Craton.

may have formed during Palaeoproterozoic NW-dipping subduction beneath the Kimberley Craton, prior to the eventual collision and amalgamation of the Kimberley Craton with the remainder of the North Australian Craton at ∼1820 Ma (Myers *et al.*, 1996; Tyler *et al.*, 1999; Griffin *et al.*, 2000). The early Proterozoic age of emplacement of some of the granites within the basement (∼1867 Ma; Gunn & Meixner, 1998) correlates with the extensive 1865–1850 Ma Whitewater Volcanics and granites of the Paperbark Supersuite that occur in the Hooper and Lamboo Complexes within the King Leopold and Halls Creek Orogens bounding the Kimberley Basin to the southwest and east respectively (Fig. 1). Granite emplacement may have been related to Palaeoproterozoic subduction beneath the region (Gunn & Meixner, 1998); however, Griffin *et al.* (2000) and Sheppard *et al.* (2001) placed the Whitewater Volcanics and the Paperbark Supersuite granites within a post-collisional tectonic setting that pre-dated the amalgamation of the Kimberley Craton with the North Australian Craton. They suggested that this felsic magmatism resulted from the collision of one or more continental fragments with the eastern margin of the Kimberley Craton, producing the temporary termination of NW-directed subduction, followed by slab collapse, lithospheric delamination, and granite production in an extensional regime (Griffin *et al.*, 2000; Sheppard *et al.*, 2001).

Overlying the granitic basement, the Kimberley and Speewah Basins contain gently folded to flat-lying Palaeoproterozoic sequences (Griffin *et al.*, 1993). The Aries kimberlite intrudes the Kimberley Group within the Kimberley Basin succession on the northern edge of the Phillips Range. Aries forms a series of three diatremes, trending N–NNE, that are infilled by massive, clast-supported, lithic-rich, volcaniclastic kimberlite breccias, and intruded by associated hypabyssal kimberlite dykes and plugs (Fig. 2). The current level of exposure of the diatremes is right on the boundary between the King Leopold Sandstone and the overlying tholeiitic basaltic lavas that comprise the Carson Volcanics (Roberts & Perry, 1969). Country rock debris from the King Leopold Sandstone and Carson Volcanics is a major component of the lithic-rich volcaniclastic breccias within the diatremes.

ANALYTICAL METHODS
Electron beam techniques

Mineral analyses were carried out on a JEOL 6400 Scanning Electron Microscope (SEM) with an Oxford instruments ISIS Energy Dispersive Spectroscopy (EDS) X-ray analytical attachment, and a JEOL 6400R electron microprobe, with an integrated Wavelength Dispersive Spectroscopy (WDS)–EDS X–ray analytical system, at the Centre for Microscopy and Microanalysis at the University of Western Australia. The operating conditions for EDS analysis include an accelerating potential of 15 kV, a beam current of 5·0 nA, a spot size of 1–2 μm and a count-time of 50 s. Peaks were calibrated to a copper standard. The operating conditions for WDS analysis include an accelerating potential of 15 kV, a beam current of 20 nA and a spot size of 1–2 μm. Element peaks were calibrated to standards that included well characterized minerals, pure metals and synthetic compounds. Analyses involved 40 s count-times on peaks and 10 s count-times on upper and lower backgrounds.

Whole-rock geochemical techniques

Whole-rock major and trace-element geochemistry was carried out by Australian Laboratory Services, Perth, Western Australia. Suitable samples of fresh hypabyssal kimberlite were selected from drill-core, crushed and pulverized. The concentrations of major and trace elements in each sample were measured using Inductively Coupled Plasma Atomic Emission Spectroscopy (ICP-AES) and Inductively Coupled Plasma Mass Spectrometry (ICP-MS) techniques, respectively. Fluorine content was determined by electrochemical techniques using a fluoride selective-ion electrode.

Laser ablation–inductively coupled plasma mass spectrometry (LA–ICP-MS)

Trace-element microanalysis of phlogopite–biotite by LA–ICP-MS was carried out on individual crystals
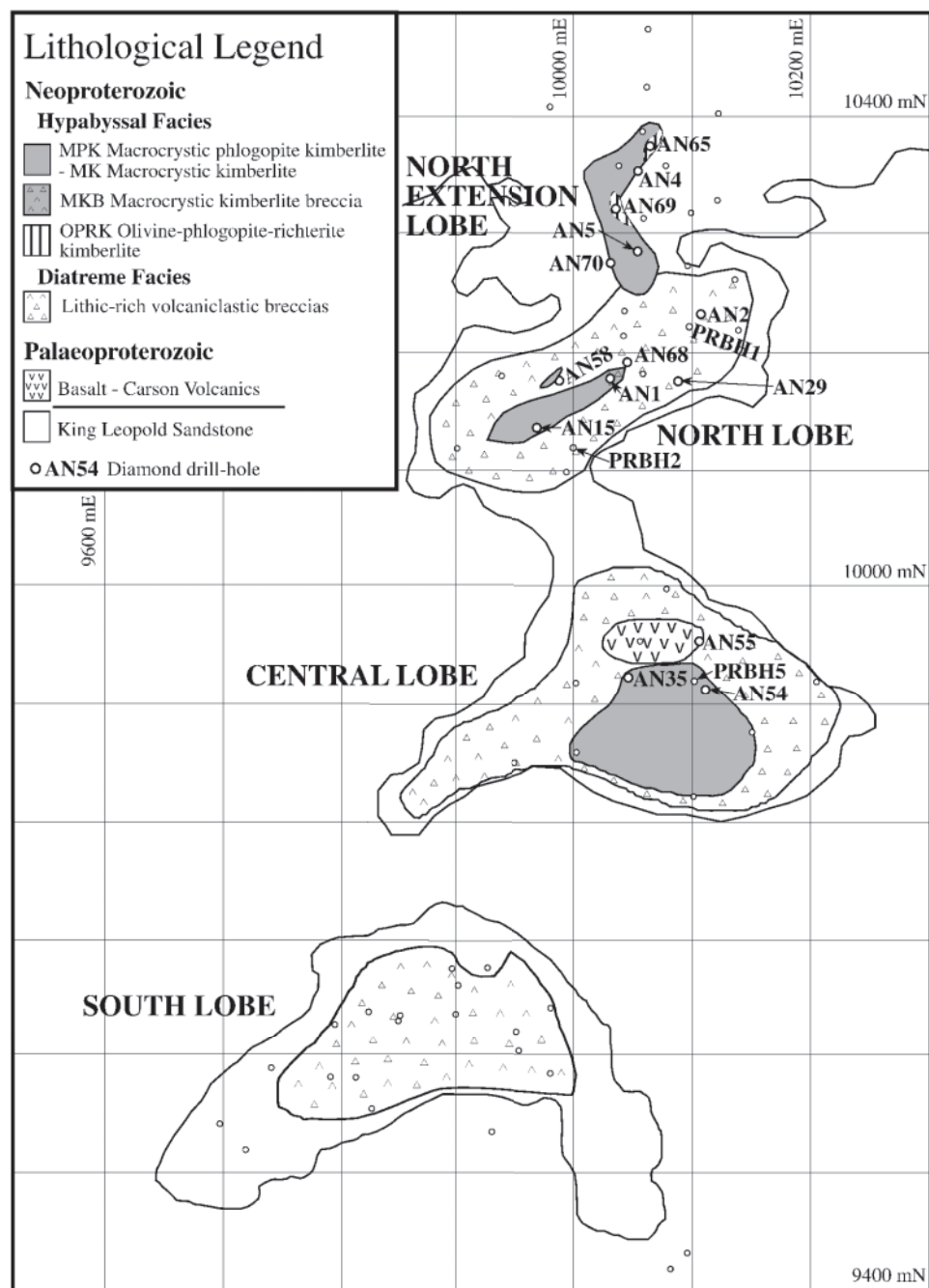
Fig. 2. Geological plan of the Aries kimberlite at the 350 m relative level, 50 m below the current surface, also showing the boundary of the diatremes at the surface, as defined by the edge of outcrop of the King Leopold Sandstone. Sample locations are indicated.

in $\sim\geq$120 µm thick sections at the Research School of Earth Sciences, Australian National University. A Hewlett Packard Agilent 7500 ICP-MS instrument coupled to an ArF Excimer UV laser ablation microprobe, operating at a wavelength of 193 nm, was used. A detailed description of the techniques employed is outlined in Eggins *et al.* (1998). Each analysis involved the measurement of backgrounds for $\sim$20 s followed by the ablation of the laser spot for $\sim$40 s, for a total period of 60 s. A recovery time was allowed to enable washout of the sample chamber between each analysis. Analyses were monitored for possible compositional heterogeneties encountered during laser ablation by the collection of data in a time-resolved graphics mode.

Standards and samples were ablated using pulse rates of 5 Hz and beam energies of ∼100 mJ per pulse. Spot diameters of ∼23 μm were used. A NIST 612 glass standard was used to obtain background and calibration measurements after every 10 analyses. Each analysis was normalized using TiO_2, which was independently determined by SEM-EDS analysis, as an internal standard.

^{40}Ar/^{39}Ar laser dating

The ^{40}Ar/^{39}Ar analyses were undertaken at the Western Australian Argon Isotope Facility, operated by a consortium consisting of Curtin University and the University of Western Australia.

Polished thick sections of 100–200 μm, mounted in Canada Balsam resin, were removed from the resin and slides by soaking in acetone. The samples underwent ultrasonic treatment in methanol and subsequently deionized water. Approximately 10 × 10 mm sections containing mica grains of interest were broken off from the polished thick sections. Samples were individually wrapped in aluminium foil, and all the samples were loaded into an aluminium package, with biotite age standard Tinto B (Rex & Guise, 1995), with a K–Ar age of 409·24 ± 0·71 Ma, being loaded at 5 mm intervals along the package to monitor the neutron flux gradient. The package was Cd-shielded and irradiated in the 5C position of the McMaster University Nuclear Reactor, Hamilton, Canada, for 90 h. Upon return, the samples were loaded into an ultra-high vacuum laser chamber with a Suprasil 2 viewport and baked to 120°C overnight to remove adsorbed atmospheric argon from the samples and chamber walls.

A New Wave Research LUV 213X 4 mJ pulsed quintupled Nd–YAG (yttrium–aluminium garnet) 213 nm UV laser, with a variable spot size of 10–350 μm, and a repetition rate of 10 Hz, was used to ablate the mineral grains. The laser was fired through a Merchantek computer-controlled X–Y–Z sample chamber stage and microscope system, fitted with a high-resolution charge coupled device camera, 6× computer controlled zoom, high magnification objective lens and two light sources for sample illumination. The gases released by laser ablation were cleaned using three SAES AP10 getter pumps to remove all active gases (e.g. CO_2, H_2O, H_2, N_2, O_2, CH_4). Remaining noble gases were equilibrated into a high sensitivity mass spectrometer (MAP 215–50), operated at a resolution of 600 and fitted with a Balzers SEV 217 multiplier. The automated extraction and data acquisition system was computer controlled, using a LabVIEW program. The mean 5 min extraction system blank Ar isotope measurements obtained during the experiments were $3·6 \times 10^{-12}$, $1·1 \times 10^{-14}$, $6·1 \times 10^{-15}$, $1·0 \times 10^{-13}$ and $3·1 \times 10^{-14}$ cm^3

STP (standard temperature and pressure) for ^{40}Ar, ^{39}Ar, ^{38}Ar, ^{37}Ar and ^{36}Ar, respectively. Samples were corrected for mass spectrometer discrimination (277·4) and nuclear interference reactions (^{39}Ar/^{37}Ar$_{Ca}$– 0·00065, ^{36}Ar/^{37}Ar$_{Ca}$– 0·000255 and ^{40}Ar/^{39}Ar$_K$– 0·0015). Errors quoted on the individual UV laser spot ages are 2σ and ^{40}Ar/^{39}Ar ages were calculated using the decay constant quoted by Steiger & Jäger (1977). J values (±0·5%) were 0·019011 for AN15-99·55m, 0·018999 for AN65-36·82m, 0·018988 for AR61, 0·018976 for AR51 and 0·018965 for AN69-59·65m.

The ^{40}Ar/^{39}Ar ages of one high-Ti phlogopite–biotite ^{40}Ar* loss profile were converted to normalized ^{40}Ar*/^{39}Ar ratios using the average 951–952 Ma grain core age (i.e. a value of 1) and the 815·4 Ma grain rim/eruption age (i.e. a value of 0) and plotted against the normalized distances from the rim of the grain. A diffusion curve was fitted through the ^{40}Ar* loss profile datapoints, assuming a cylindrical diffusion geometry, which is appropriate for micas (Hames & Bowring, 1994), and using the Ar diffusion parameters of phlogopite (Giletti, 1974) and biotite (Grove & Harrison, 1996), using the method described by Wartho & Kelley (2003). In general, all the mica grains ^{40}Ar/^{39}Ar analysed in these samples were small (e.g. 188–1185 μm)— much smaller than mica grains analysed in previous studies in southern Africa, the Solomon Islands and Russia (Pearson *et al.*, 1997; Kelley & Wartho, 2000; Kempton *et al.*, 2001; Wartho & Kelley, 2003).

PETROGRAPHY

The mineralogy and petrology of the Aries kimberlite was originally described in detail by Edwards *et al.* (1992) using material obtained from eight diamond drill-holes that had sampled the kimberlite to depths of ≤100 m. Their petrographic and mineralogical descriptions were based on samples from the central (PRBH 5, PRBH 17), north (PRBH 1, PRBH 2) and north extension (PRBH 45) lobes. Samples from the South Lobe diatreme were not described because the hypabyssal lithologies were heavily altered. Edwards *et al.* (1992) recognized four lithologies: (1) uniformly textured medium-grained macrocrystal rock (Lithology 'M'— 'Medium') that comprises 30–40% olivine macrocrysts and microphenocrysts in a uniformly textured, phlogopite-rich groundmass that includes apatite, titanite, spinels and deuteric minerals; (2) uniformly textured aphanitic macrocrystal rock (Lithology 'A'— 'Aphanitic'), consisting of ≤5% olivine macrocrysts and microphenocrysts in a fine-grained, phlogopite-rich groundmass that includes interstitial calcite and serpentine; (3) macrocrystal segregated rock (Lithology 'S'—'Segregated'), a phlogopite-rich lithology that

includes irregularly shaped groundmass segregations of calcite and serpentine; (4) breccias rich in country-rock xenoliths. On the basis of our new petrological studies, we have combined the first three lithologies into one hypabyssal lithofacies, termed a 'macrocrystic phlogopite kimberlite' (MPK); however, we also recognize a sub-facies—a globular segregationary-textured macrocrystic kimberlite (SK), in which a globular segregationary-textured groundmass is well developed. This texture can be easily recognized by macroscopic examination of the drill-core.

Edwards *et al.* (1992) also described the chemical zonation of phlogopite phenocrysts from the hypabyssal lithologies. Rare phlogopite phenocrysts preserve up to four distinct growth zones (zones 1–4) from the core to the rim, which can be distinguished on the basis of major-element chemistry (see discussion below). Most phenocrysts only have cores of zone 2 composition overgrown by zone 4 rims (Fig. 3a). In this study, we have recognized a number of new varieties of mica from the MPK, and several mantle and crustal xenoliths, and explore the implications of this phenocryst zonation for the magmatic evolution of the kimberlite.

Samples of hypabyssal kimberlite and altered mantle and crustal xenoliths that were used for petrographic examination and microanalysis in this study came from diamond drill-holes (DDH) AN 35, 54, 55 in the central lobe; DDH AN 1, 2, 15, 29, 58, 68 in the north lobe; and DDH AN 4, 5, 65, 69, 70 in the north extension lobe (Fig. 2). These samples range in depth from 25 to 285 m. Within the three diatremes, units of hypabyssal kimberlite most often preserve fresh minerals, free from deuteric or hydrothermal alteration, or oxidation because of weathering, which are suitable for microanalysis. Units of volcaniclastic kimberlite are commonly strongly hydrothermally altered or oxidized, and their primary mineralogy is only rarely preserved. Thus, we concentrated on the mineralogy of the relatively fresh hypabyssal kimberlite intrusions in this study. No samples of hypabyssal kimberlite from the south lobe diatreme proved to be suitable for microanalysis because of the degree of weathering and alteration in this lobe.

The following sections describe the different hypabyssal kimberlite and xenolith lithologies encountered in the Aries diatremes.

Macrocrystic phlogopite kimberlite (MPK), macrocrystic kimberlite (MK), macrocrystic kimberlite breccia (MKB) and globular segregationary-textured macrocrystic kimberlite (SK)

Hypabyssal kimberlite dykes and plugs, with widths ranging from several centimetres to ~70 m, intrude each of the lobes of the Aries kimberlite (Fig. 2). Macrocrystic phlogopite kimberlite (MPK) dykes generally have sharp intrusive contacts and cross-cutting relationships with the surrounding volcaniclastic breccias and country rocks. Smaller dykes and stringers of MPK, generally tens of centimetres to <1 m wide, may be highly irregular and discontinuous in form. Hypabyssal MPK has an inequigranular or macrocrystic texture, in which ≤20 mm olivine macrocrysts and ≤4 mm phenocrysts comprise ≤50% of the rock. The olivine content is generally low, consisting of <10% macrocrysts and <20% phenocrysts. MPK also contains a population of euhedral–subhedral phlogopite phenocrysts, ranging up to ~10% in abundance and up to ~1·5 mm long (Fig. 3a–d, f, j). These macrocrysts and phenocrysts are set in a variably fine- to coarse-grained phlogopite-rich groundmass composed of randomly orientated phlogopite laths up to 3 mm long in coarse-grained zones. The groundmass also contains variable amounts of spinel (magnesiochromite to magnetite; ≤30% in abundance), serpentine, talc, calcite, diopside ± fluorapatite, along with a diverse accessory mineral assemblage that is detailed in Table 1. The margins of the MPK dykes are commonly aphanitic, containing <5% olivine macrocrysts. Aphanitic zones at dyke margins are generally <8 cm wide, but can be up to 28 cm in width. Olivine-rich bands and aphanitic zones, up to 40 cm wide, also occur within dykes away from their margins.

The groundmass of MPK contains widespread segregationary textures, and is transitional to globular segregationary-textured kimberlite (SK) in some regions. In general, groundmass segregations in MPK are irregularly shaped areas, up to ~10 mm wide, infilled with serpentine, calcite, phlogopite and/or fluorapatite, with or without minor diopside, magnetite, ilmenite–pyrophanite, pyrite, chalcopyrite and/or galena (Fig. 4a). These segregations have relatively sharp boundaries with the surrounding uniform-textured groundmass. Crystals of apatite and/or phlogopite, each ≤1 mm long, commonly intrude from the margins of segregations into their interiors. A sample of MPK from the north lobe (AN15-124·04m) contains segregated veinlets and patches in the groundmass (<8 mm long), that contain <1 mm long inclusion-rich crystals of diopside, ≤0·3 mm long subhedral, equant crystals of andradite, serpentine, apatite, magnetite (≤0·1 mm long), calcite and rare phlogopite (Fig. 4d).

Macrocrystic kimberlite (MK) refers to hypabyssal kimberlite that has a macrocrystic texture, but in which the primary mineral assemblage of macrocrystic phlogopite kimberlite has been extensively altered and replaced by quartz, serpentine–talc, chlorite, clay and/or carbonate. Hypabyssal MPK or MK that contains ≥15% country-rock xenoliths is classified as macrocrystic kimberlite breccia (MKB).

Olivine–phlogopite–richterite kimberlite (OPRK)

Massive hypabyssal MPK exposed in the north extension lobe varies in composition to an olivine–phlogopite–richterite kimberlite (OPRK) adjacent to the walls of the lobe (Fig. 2). The OPRK contains potassian richterite, diopside and/or sanidine as fine-grained granular groundmass phases, and may include ≤1 mm long euhedral–subhedral poikilitic potassian richterite laths. Similar to MPK, OPRK contains up to ~10%
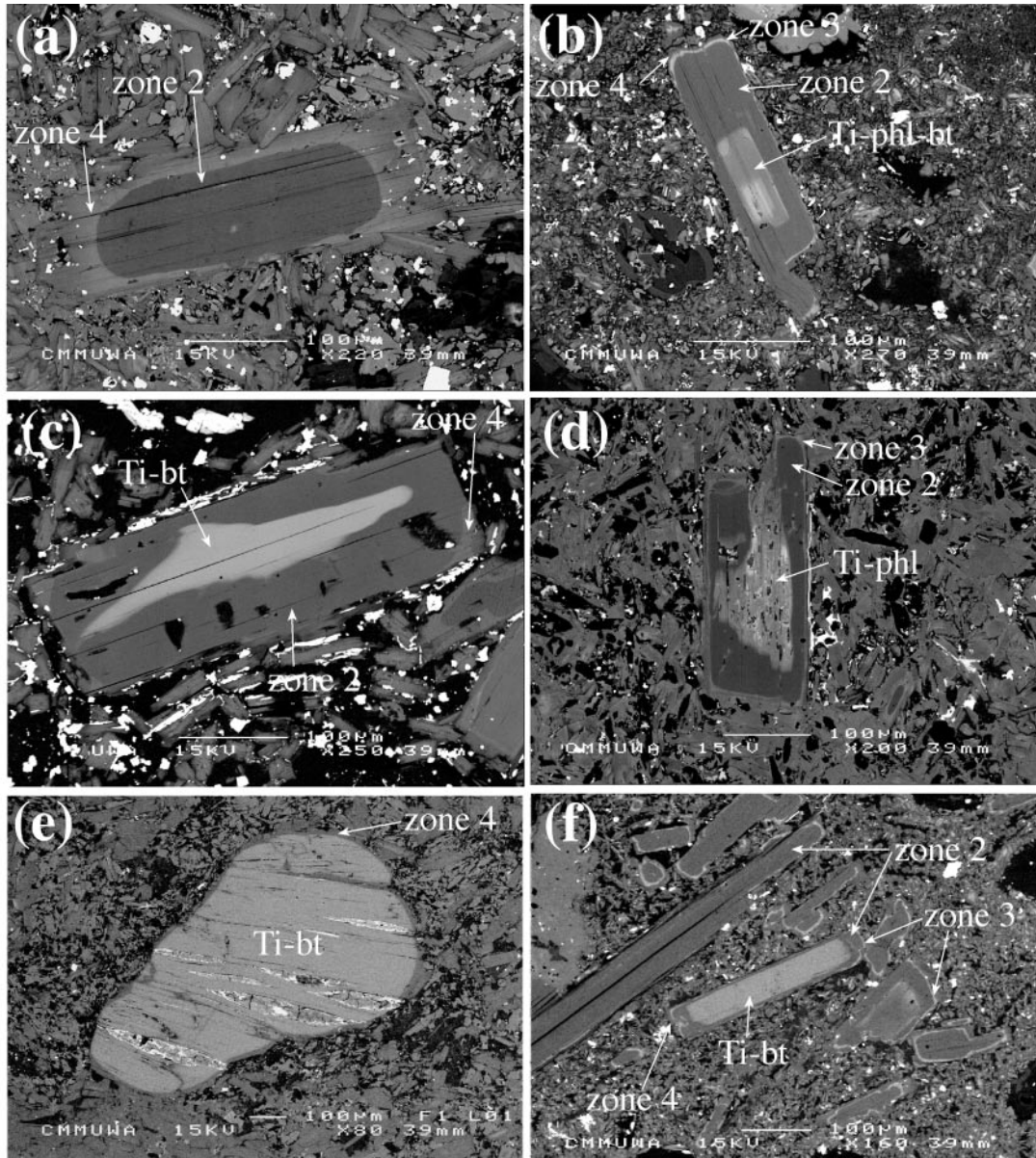
Fig. 3. Back-scattered electron (BSE) images of phlogopite–biotite macrocrysts and phenocrysts: (a) phlogopite phenocryst (zone 2) overgrown by brighter zone 4 phlogopite rim in MPK (AN–99·55m); (b) phlogopite phenocryst in MPK (AN15-99·55m) containing a variable high-Ti phlogopite to high-Ti biotite core (Ti–phl–bt) that was overgrown by zone 2 phlogopite, and thin zone 3 (bright) and zone 4 phlogopite rims; (c) resorbed high-Ti biotite macrocryst (Ti–bt) overgrown by zones 2 and 4 phlogopite in MPK (AN54-205·92m); (d) sieve–textured, resorbed high-Ti phlogopite macrocryst (Ti–phl) overgrown by zone 2 and zone 3 phlogopite rims in OPRK (AN69-59·44m); (e) high-Ti biotite macrocryst overgrown by zone 4 phlogopite in MPK (AN4-149·95m); (f) high-Ti biotite macrocryst overgrown by zones 2–4 phlogopite, and zone 2 phlogopite phenocrysts with zone 3–4 rims in MPK (AN15-95·77m); (g) high-Ti biotite macrocryst with zone 2 and 3 overgrowth rims in OPRK (AN65-36·82m); (h) deformed high-Ti biotite macrocryst (bt 2) in MPK (AN54-85·94m); (i) F-rich, high-Mg phlogopite xenocryst, with a zone 4 phlogopite overgrowth rim and Fe–oxide alteration along cleavage planes, in MPK (AN54-132·3m); (j) phlogopite phenocryst in MPK (AN55-131·57m) that contains a zone 1 phlogopite core, overgrown by zones 2 and 4 phlogopite.

Fig. 3. Continued

phlogopite phenocrysts by volume (<0·5 mm long). The groundmass of OPRK is commonly fine-grained and varies from phlogopite-rich to diopside–amphibole-rich on a millimetre scale. OPRK is also distinguished by the morphology of the contained olivine macrocrysts and phenocrysts; the ≤5 mm diameter macrocrysts are typically sparse (<5% in abundance), and co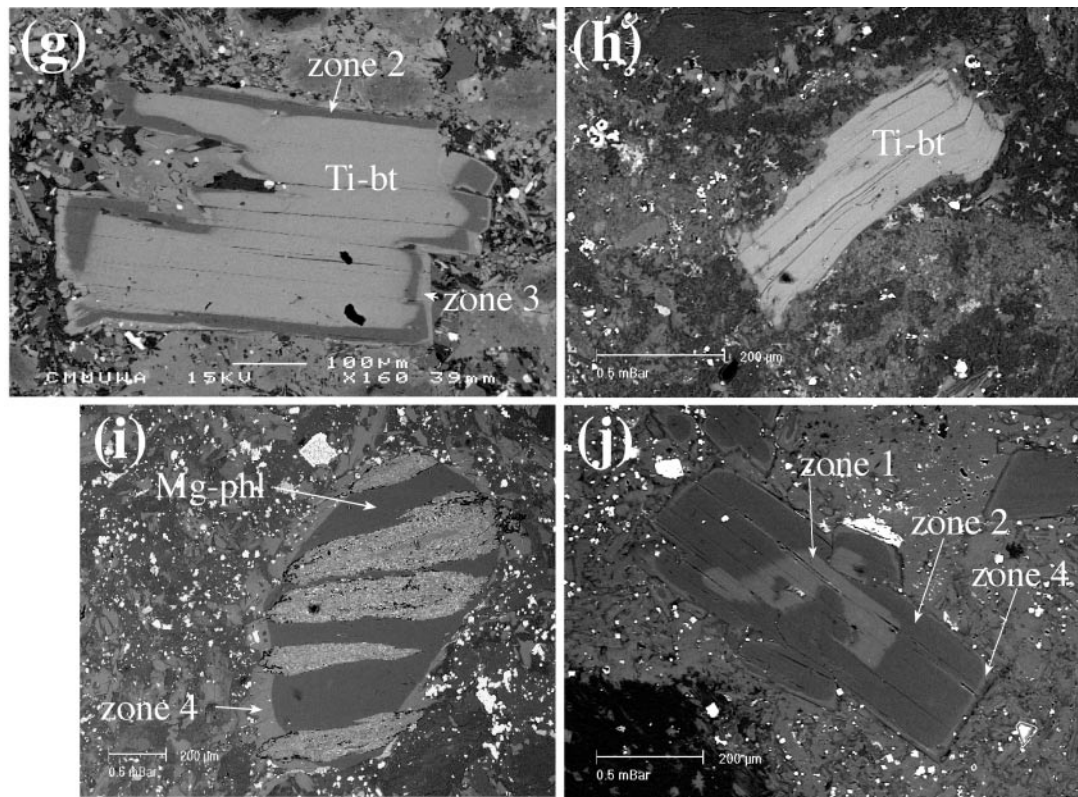mmonly exhibit resorption features such as heavily embayed margins; the abundant (<30%) ≤2 mm long euhedral phenocrysts may form twins and complex saw-tooth crystal groups. As there is a lack of sharp, well defined contacts between OPRK and MPK, the relative timing of intrusion could not be defined, and the precise relationship between the two units remains uncertain, but may be gradational.

The texture of the groundmass in OPRK varies from uniform to segregationary. Groundmass segregations range from ~1 to 12 mm in length, and contain varying proportions of ≤1 mm long amphibole, phlogopite, fluorapatite and/or diopside crystals, surrounded by serpentine, sanidine, calcite and/or siderite, along with minor titanite, chalcopyrite ± rare quartz (Fig. 4b). These segregations are irregularly shaped areas within the groundmass that have relatively sharp boundaries, grading into the surrounding groundmass over tens of millimetres. The euhedral to subhedral amphibole crystals vary in composition from potassic richterite to magnesio–arfvedsonite or actinolite, and often intrude from the margins of segregations into their interiors. The volume of amphibole in different segregations varies from <10 to ~90%.

Macrocrystic serpentine–diopside ultramafic dykes (MSDU)

Several narrow macrocrystic serpentine–diopside ultramafic dykes (MSDU), each <1 m wide, intrude the MPK in the north extension lobe (DDH AN4). These ultramafic dykes contain ≤40% rounded olivine macrocrysts, up to ~10 mm in diameter, separated by interstitial crystals of diopside (<2 mm wide), some of which are poikilitic and enclose olivine macrocrysts, along with serpentine, and <2 mm wide spinel grains (chromite to magnetite), minor fluorapatite, phlogopite, calcite, allanite–(Ce), monazite–(Ce) and aeschynite–(Ce). These dykes are only observed in DDH AN4 and thus appear very limited in extent. They have sharp intrusive contacts with the surrounding macrocrystic phlogopite kimberlite.

Table 1: Petrography of the Aries kimberlite

	Macrocrysts–phenocrysts	Groundmass	Groundmass segregations
Macrocrystic phlogopite kimberlite (MPK)	≤50% ol mac + phen (generally low: ≤10% mac + ≤20% phen) <10% phlog phen spinel-chromite xenocrysts	phlog, chromite-magnetite, calcite, serp, talc, Sr-apatite, titanite, diop: TiO_2 ≤1·52 wt %, Al_2O_3 ≤0·94 wt %, Na_2O ≤1·37 wt %, aeschynite-(Ce), barite, monazite-(Ce), rutile–niobian rutile, siderite, py, cpy, galena, Ni sulphides, andradite, hydrogarnet	phlog, Sr-apatite, calcite, serpentine, py, cpy, galena, monazite-(Ce), ilmenite-pyrophanite
Olivine–phlogopite richterite kimberlite (OPRK)	< 10% ol mac < 30% ol phen, including complex crystal aggregates and twins, <10% phlog phen, spinel-chromite xenocrysts	phlog, potassian richterite, diop: TiO_2 0·26–1·66 wt %, Al_2O_3 ≤0·71 wt %, Na_2O 0·45–2·5 wt % san (BaO ≤3·56 wt %), Sr-apatite, chromite-magnetite, cpy	potassic richterite, magnesio-arfvedsonite, actinolite, phlog, diop, san, Sr-apatite, serp, siderite, calcite, titanite, cpy, quartz
Macrocrystic serpentine–diopside ultramafic dykes (MSDU)	<40% ol mac + phen	serp, diop: TiO_2 0·28–1·67 wt %, Al_2O_3 ≤0·82 wt %, Na_2O ≤1·47 wt %, chromite-magnetite, Sr-apatite, phlog, allanite-(Ce), monazite-(Ce), aeschynite-(Ce)	–

mac, macrocrysts; phen, phenocrysts; ol, olivine; phlog, phlogopite; diop, diopside; serp, serpentine; san, sanidine; py, pyrite; cpy, chalcopyrite; Sr-apatite, Sr-bearing fluorapatite.

Phlogopite–biotite-bearing serpentinized ultramafic xenoliths

Three serpentinized ultramafic xenoliths (AN29-234·15m, AR51, AR61) that contain grains of high-Ti phlogopite–biotite were found in DDH AN29 in the north lobe (Fig. 2). Red-brown to dark-brown high-Ti phlogopite–biotite occurs either as minor (≤0·8 mm long) euhedral–subhedral laths, or as ≤1 mm long anhedral grains, both occurring at former grain boundaries between silicate minerals. The other silicate minerals in these xenoliths have been completely replaced by serpentine–talc, but the original grain boundaries are still evident and each xenolith has a coarse-grained, equigranular texture. The complete replacement of all silicate minerals, apart from high-Ti phlogopite–biotite, by serpentine–talc suggests that the original rocks were ultramafic in composition. Minor anhedral grains of rutile that are ≤0·7 mm long, also occur at former grain boundaries, and are associated with the high-Ti phlogopite–biotite grains in all three xenoliths. One xenolith (AR61) contains minor apatite (≤0·4 mm) and very rare grains of zircon (≤0·2 mm wide).

RESULTS
Mineral chemistry

The composition of phlogopite–biotite is focused on in this study because of the insights into magma evolution provided by the chemical zonation of the phlogopite–biotite phenocrysts and the composition of high-Ti phlogopite–biotite macrocrysts, as described above. In an effort to define more precisely the provenance of the various mica macrocrysts and xenocrysts that occur in the MPK and the OPRK, LA–ICP-MS trace-element data were obtained for phlogopite–biotite macrocrysts and phenocrysts (zones 1 and 2 composition) from the MPK and the OPRK lithofacies, and phlogopite–biotite grains from a granite (AN69-59·65m) and a serpentinized ultramafic xenolith (AR51). Amphiboles in the OPRK also show significant chemical variation, and this is important in rock classification and in understanding the differentiation of the kimberlite magmas. The compositions of minor silicate phases, including diopside, sanidine and andradite, are summarized in Tables 1 and 2. The oxide mineralogy of the groundmass of the kimberlite was described in detail by Edwards *et al.* (1992); new data for spinels occurring in the groundmass and in mantle xenoliths are the subject of a separate paper (Downes *et al.*, in preparation).

Texture and composition of phlogopite–biotite
High-Mg phlogopite xenocrysts

The MPK contains rare ≤1 mm long euhedral–subhedral xenocrysts of F-rich (1·31–3 wt %), highly
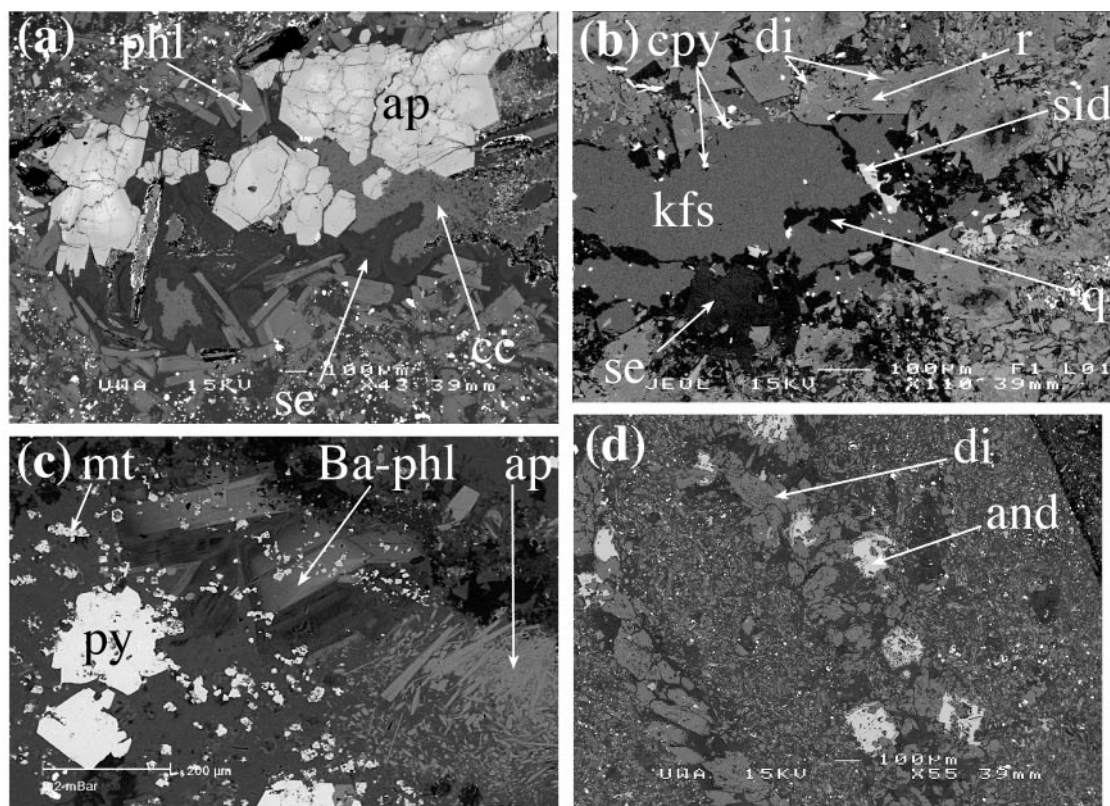
Fig. 4. BSE images of groundmass segregations in MPK and OPRK: (a) a fluorapatite (ap), phlog (phl), serpentine (se), calcite (cc) filled segregation in MPK (AN54-132·3m); (b) groundmass segregation in OPRK (AN65-36·82m; kfs, potassium feldspar; di, diopside; r, richterite; q, quartz; sid, siderite; cpy, chalcopyrite); (c) barian phlogopite (Ba–phl) in groundmass segregation in MPK (AN55-131·57m; py, pyrite; mt, magnetite); (d) diopside (di)–andradite (and) veinlets in MPK (AN15-124·04m).

magnesian phlogopite (Mg-number 95·3–98·5, Al_2O_3 15·3–17·13 wt %; Table 3; Fig. 5a, b) that is colourless and non-pleochroic in thin section. In samples from the central and north lobes, these phlogopite xenocrysts are overgrown by thin, continuous, orange-brown rims of phlogopite (Fig. 3i).

Trace-element data for one of these xenocrysts in a MPK sample from the central lobe (AN55-131·57m) indicate that it contains low levels of most minor elements (Nb, Zr, Rb, Sr, Co, Ni, Zn, Li, Ba, Y) compared with the other analysed phlogopite–biotites from the Aries kimberlite (Table 4; Fig 6a–f).

High-Ti phlogopite–biotite macrocrysts

Both the MPK and OPRK contain minor ≤1·1 mm long macrocrysts of red-brown (bt 1) and dark-brown (bt 2) high-Ti biotite, that vary in morphology from subhedral to strongly resorbed, and generally are overgrown by later generations of phlogopite (zones 2, 3, 4; Fig. 3c, e–h). Rare high-Ti biotite xenocrysts (bt 2), some of which are deformed, are more Fe-rich than the red-brown high-Ti biotite (bt 1) macrocrysts and are not overgrown by later generations of phlogopite (Figs 3h, 5a).

Rare dark-brown high-Ti phlogopite macrocrysts, ≤0·9 mm long, have similar subhedral to strongly resorbed habits to the high-Ti biotite macrocrysts (bt 1). These grains are similarly overgrown by later generations of phlogopite (Fig. 3b, d). There is some overlap in composition with phlogopite from two of the serpentinized ultramafic xenoliths recovered from Aries, in terms of Al–Fe–Ti content (Fig. 5a, b; Table 3). One high-Ti phlogopite macrocryst was analysed to determine its trace-element content and it is distinguishable by its relatively high Nb (84–109 ppm; Fig. 6a, c), Sr (76–99 ppm; Fig. 6d), Co (94–104 ppm), Li (33·7–45·2 ppm) and Ba (6157–7494 ppm) contents (Table 4). Very rare high-Ti phlogopite macrocrysts have sieve textures (Fig. 3d) and contain numerous small inclusions such as high-Al micas. A dissolution texture seen in high-Ti phlogopite macrocrysts in the OPRK is characterized by the crystallization along cleavage planes, of groundmass serpentine, chalcopyrite and sanidine grains, enclosing <100 μm long rectangular fragments of the larger phlogopite macrocryst.

Table 2: Representative electron microprobe analyses of amphibole, sanidine and andradite from the Aries kimberlite.

Sample	AN65-54·3 m	AN65-54·3 m	AN65-54·3 m	AN65-54·3 m	AN65-54·3 m		AN65-36·82A	AN65-36·82A	AN15-124·04 m	AN15-124·04 m
Analysis	65a3c	65a19c2	65a19r	65a22c	65a22r		65-3682akfs7	65-3682akfs11	15gt1c	15gt2c
Position	groundmass	segregation	segregation	segregation	segregation		segregation	groundmass		
Mineral	potassian richt	potassic richt	actinolite	mag-arfved	mag-arfved		sanidine	sanidine	andradite	andradite
F	1·48	0·48	0·00	0·25	0·33	MgO	n.d.	n.d.	1·42	0·79
MgO	18·82	14·54	13·38	12·41	14·07	Al_2O_3	19·62	19·67	1·04	2·1
Al_2O_3	1·78	0·36	0·70	0·05	0·14	SiO_2	63·91	63·61	31·96	34·72
SiO_2	54·47	54·03	52·84	52·82	53·88	Na_2O	0·55	1·75	0·05	0·09
Na_2O	5·84	5·51	0·17	6·58	7·37	K_2O	15·74	13·20	0	0·02
K_2O	1·75	3·65	0·42	3·38	3·34	CaO	0·01	0·06	33·67	33·87
CaO	6·23	3·78	11·70	2·23	0·84	TiO_2	n.d.	n.d.	7·66	1·73
TiO_2	1·09	0·48	0·06	0·66	0·57	Cr_2O_3	n.d.	n.d.	0·11	0
Cr_2O_3	0·16	0·11	0·06	0·10	0·08	MnO	n.d.	n.d.	0·09	0·12
MnO	0·19	0·47	1·62	0·76	0·30	Fe_2O_3	0·11	0·79	24·7	26·5
FeO	7·52	13·64	14·59	15·82	14·15	BaO	0·17	2·01	n.d.	n.d.
Nb_2O_5	0·04	0·06	0·21	0·31	0·14	TOTAL	100·10	101·09	100·71	99·94
Total	99·35	97·10	95·72	95·37	95·20	Structural Formula 32 O			12 O	
Structural Formula 23 O						Mg	n.d.	n.d.	0·18	0·1
F	0·66	0·23	0·00	0·12	0·16	Al	4·27	4·28	0·1	0·21
Mg	3·98	3·22	2·98	2·83	3·16	Si	11·81	11·75	2·67	2·91
Al	0·30	0·06	0·12	0·01	0·03	Na	0·2	0·63	0·01	0·01
Si	7·74	8·03	7·90	8·08	8·14	K	3·71	3·11	0	0
Na	1·61	1·59	0·05	1·95	2·16	Ca	0	0·01	3·01	3·04
K	0·32	0·69	0·08	0·66	0·64	Ti	n.d.	n.d.	0·48	0·11
Ca	0·95	0·60	1·87	0·37	0·14	Cr	n.d.	n.d.	0·01	0
Ti	0·12	0·05	0·01	0·08	0·07	Mn	n.d.	n.d.	0·01	0·01
Cr	0·02	0·01	0·01	0·01	0·01	Fe	0·01	0·04	1·55	1·67
Mn	0·02	0·06	0·21	0·10	0·04	Ba	0·01	0·15	n.d.	n.d.
Fe	0·89	1·69	1·82	2·02	1·79	Total	20	19·96	8·02	8·05
Nb	0·00	0·00	0·01	0·02	0·01					
Total	16·61	16·24	15·07	16·23	16·33					
Na/K	5·09	2·30	0·63	2·96	3·35					
A.I.	6·48	36·74	1·05	260·90	112·00					
Al/Si	0·04	0·01	0·02	0·001	0·003					

A.I. (Agpaitic index) = $(Na_2O + K_2O)/Al_2O_3$ atomic proportions; richt, richterite; mag-arfved, magnesioarfvedsonite; n.d., not determined.

Table 3: Representative electron microprobe and SEM-EDS analyses of phlogopite-biotite from the Aries kimberlite (electron microprobe WDS analyses are those in which BaO and F have been determined)

Sample	AN29-236·21m (AR51)	AN29-265·85m (AR61)	AN29-234·15m	AN69-59·65m	AN55-131·57m	AN55-131·57m	AN55-131·57m	AN55-131·57m	AN55-131·57m	AN55-131·57m	AN55-131·57m
Lobe	north	north	north	north ext	central	central	central	central	central	central	central
Position	core	core	core	core	core	rim	core	core	core	mid	core gmass
Mica type	phlog in xen	bt in xen	phlog in xen	bt in xen	Ba-phlog	Ba-phlog	bt1 mac	z2 phlog	z1 phlog	z2 phlog	z4 phlog
Rock type	serp umafic xen	serp umafic xen	serp umafic xen	granite xen	MPK	MPK	MPK	MPK	MPK	MPK	MPK
SiO_2	39·25	37·45	37·62	34·6	33·59	31·99	37·31	40·66	38·58	40·53	39·56
TiO_2	5·19	5·36	5·33	5·56	0·25	0·38	5·36	1·39	2·66	1·45	2·08
Al_2O_3	13·29	14·15	14·59	15·98	18·8	18·98	14·43	13·24	14·98	13·38	12·55
Cr_2O_3	0·32	0·27	0	0	0·22	0·13	0·43	1·65	0·25	1·29	0·11
FeO	8·87	13·75	10·68	22·64	2·3	2·02	17·14	4·56	9·52	4·67	7·42
MnO	0	0	0	0	0	0	0·03	0·04	0·09	0·07	0·14
MgO	17·89	14·16	15·97	7·24	24·67	24·24	12·07	23·84	19·28	23·7	22·86
CaO	0	0	0	0	0·02	0	0·01	0·04	0·05	0·02	0·19
Na_2O	0	0·33	0·45	0	0·1	0·13	0·19	0·32	0·81	0·4	0·12
K_2O	10·15	10·04	9·79	9·67	6·77	5·9	9·45	9·86	9·03	9·91	9·53
BaO	n.d.	n.d.	n.d.	n.d.	10·2	12·68	0·27	0·44	0·57	0·49	1·08
F	n.d.	n.d.	n.d.	n.d.	0·72	0·93	0·42	1·01	0·54	0·81	1·37
Total	94·96	95·51	94·43	95·69	97·63	97·36	97·09	97·04	96·34	96·73	97·03
Mg-number	78·2	64·7	72·7	36·3	95·0	95·5	55·7	90·3	78·3	90·0	84·6

Sample	AN65-36·82A	AN65-36·82A	AN65-36·82m	AN65-36·82m	AN65-36·82m	AN65-54·3m	AN69-59·44m	AN69-59·44m	AN69-59·44m
Lobe	north ext	north ext	north ext	north ext	north ext	north ext	north ext	north ext	north ext
Position	core	Core	core	mid	rim	core	core	mid	rim
Mica type	bt1 mac	bt1 mac	bt1 mac	z2 phlog	z3 bt	z2 phlog	phlog mac	z2 phlog	z3 phlog
Rock type	OPRK	OPRK	OPRK	OPRK	OPRK	OPRK	OPRK	OPRK	OPRK
SiO_2	36·51	36·32	36·46	37·24	36·55	37·9	37·8	39·34	38·83
TiO_2	4·48	5·29	5·5	1·59	5·81	1·37	5·58	1·87	3·03
Al_2O_3	15·25	14·49	13·97	13·6	10·9	14·38	14·73	14·37	12·43
Cr_2O_3	0·06	0·24	0	1·14	0·21	1·33	0·26	1·15	0
FeO	15·01	16·97	17·67	6·22	16·24	5·25	13·59	5·81	11·83
MnO	0	0	0	0·11	0·26	0·06	0	0	0·19
MgO	15·46	12·9	12·07	21·14	13·97	23·89	15·09	23·18	19·59
CaO	0·02	0·01	0	0	0	0·03	0	0	0
Na_2O	0·25	0·2	0·48	0·41	0·59	0·51	0	0	0
K_2O	9·21	9·04	9·73	9·95	9·01	9·94	10·26	10·42	10·11
BaO	0·61	0·52	n.d.	n.d.	n.d.	0·7	n.d.	n.d.	n.d.
F	0·36	0·48	n.d.	n.d.	n.d.	1·29	n.d.	n.d.	n.d.
Total	97·2	96·46	95·95	91·4	93·54	96·64	97·31	96·14	96·01
Mg-number	64·7	57·5	54·9	85·8	60·5	89·0	66·4	87·7	74·7

Sample	AN15-124·04m	AN15-124·04m	AN15-124·04m	AN15-108·06m	AN15-108·06m	AN15-108·06m	AN15-108·06m	AN15-195·27m	AN15-195·27m	AN15-95·77m
Lobe	north	north	north	north	north	north	north	north	north	north
Position	core	core	Core	core	mid	rim	core	core	core	mid
Mica type	Mg-phlog	phlog mac	z2 phlog	z1 phlog	z2 phlog	z4 phlog	bt1 mac	phlog mac	phlog mac	z1 phlog
Rock type	MPK	MPK	MPK	MPK	MPK	MPK	MPK	MPK	MPK	MPK
SiO_2	40·46	38·78	37·39	38·31	38·77	38·06	35·6	37	36·44	37·87
TiO_2	0·31	4·95	1·36	2·61	1·41	2·04	4·92	5·44	2·85	2·49
Al_2O_3	16·25	13·85	14·43	15·74	13·77	12·62	13·93	14·56	13·83	14·06
Cr_2O_3	0	0·28	1·53	0·35	1·31	0·16	0·29	0·7	0·1	0·09
FeO	0·86	11·35	5·51	6·2	5·18	7·65	15·7	10·02	11·19	10·92
MnO	0	0	0·06	0	0·09	0	0·07	0·13	0·18	0·11
MgO	27·01	17·93	24·02	22·76	24·36	24·58	13·32	17·37	18·41	19·2
CaO	0·04	0·01	0·07	0·04	0·04	0·12	0·05	0·03	0·03	0·05
Na_2O	0·49	0·2	0·43	0·09	0·13	0·04	0·15	0·21	0·73	0·56
K_2O	10·48	10·48	9·48	10·65	10·71	9·59	9·93	10·44	9·73	10·18
BaO	0·18	0·14	0·58	0·71	0·44	1·72	0·11	0·72	0·71	0·49
F	2·93	1·84	0·79	1·12	1·05	1·44	1·02	0·7	0·5	0·53
Total	99·01	99·79	95·75	98·58	97·25	98·01	95·09	97·31	94·69	96·56
Mg-number	98·2	73·8	88·6	86·7	89·3	85·1	60·2	75·5	74·6	75·8

Table 3: continued

Sample	AN15-99·55m	AN15-99·55m	AN15-99·55m	AN15-99·55m	AN15-99·55m	AN15-99·55m	AN15-99·55m	AN15-99·55m
Lobe	north	north	north	north	north	north	north	north
Position	core	mid	Rim	core	core	core	mid	rim
Mica type	phlog mac	z2 phlog	z4 phlog	bt1 mac	bt1 mac	phlog mac	z2 phlog	z3 phlog
Rock type	MPK	MPK	MPK	MPK	MPK	MPK	MPK	MPK
SiO_2	36·93	39·32	39·83	37·22	37·07	40·97	39·82	37·18
TiO_2	2·68	1·57	2·12	3·84	4·28	2·11	1·44	3·7
Al_2O_3	13·64	13·74	11·16	13·66	13·62	11·93	13·7	10·82
Cr_2O_3	0·17	1·32	0	0	0	0·16	1·63	0
FeO	11·34	4·89	9·04	17·56	16·41	11·07	4·69	14·85
MnO	0	0	0·38	0·2	0	0·21	0	0·33
MgO	18·72	23·33	22·65	14·93	15·17	20·78	23·87	18·19
CaO	0	0	0	0	0	0	0	0
Na_2O	0·32	0·34	0	0·45	0	0·8	0	0
K_2O	9·75	10·25	10·43	9·21	9·64	9·04	10·56	9·45
BaO	n.d.	n.d.	n.d.	n.d.	n.d.	n.d.	n.d.	n.d.
F	n.d.	n.d.	n.d.	n.d.	n.d.	n.d.	n.d.	n.d.
Total	93·55	94·76	95·61	97·07	96·19	97·07	95·71	94·52
Mg-number	74·6	89·5	81·7	60·2	62·2	77·0	90·1	68·6

Mg number = $100*(Mg/Mg + Fe_{tot})$. n.d., not determined; phlog, phlogopite; bt, biotite; xen, xenolith; mac, macrocryst; z1/2/3/4, zone 1/2/3/4; Ba-phlog, barian phlogopite; Mg-phlog, high-Mg phlogopite; ext, extension; serp, serpentinized; umafic, ultramafic; gmass, groundmass; 0 indicates below detection.
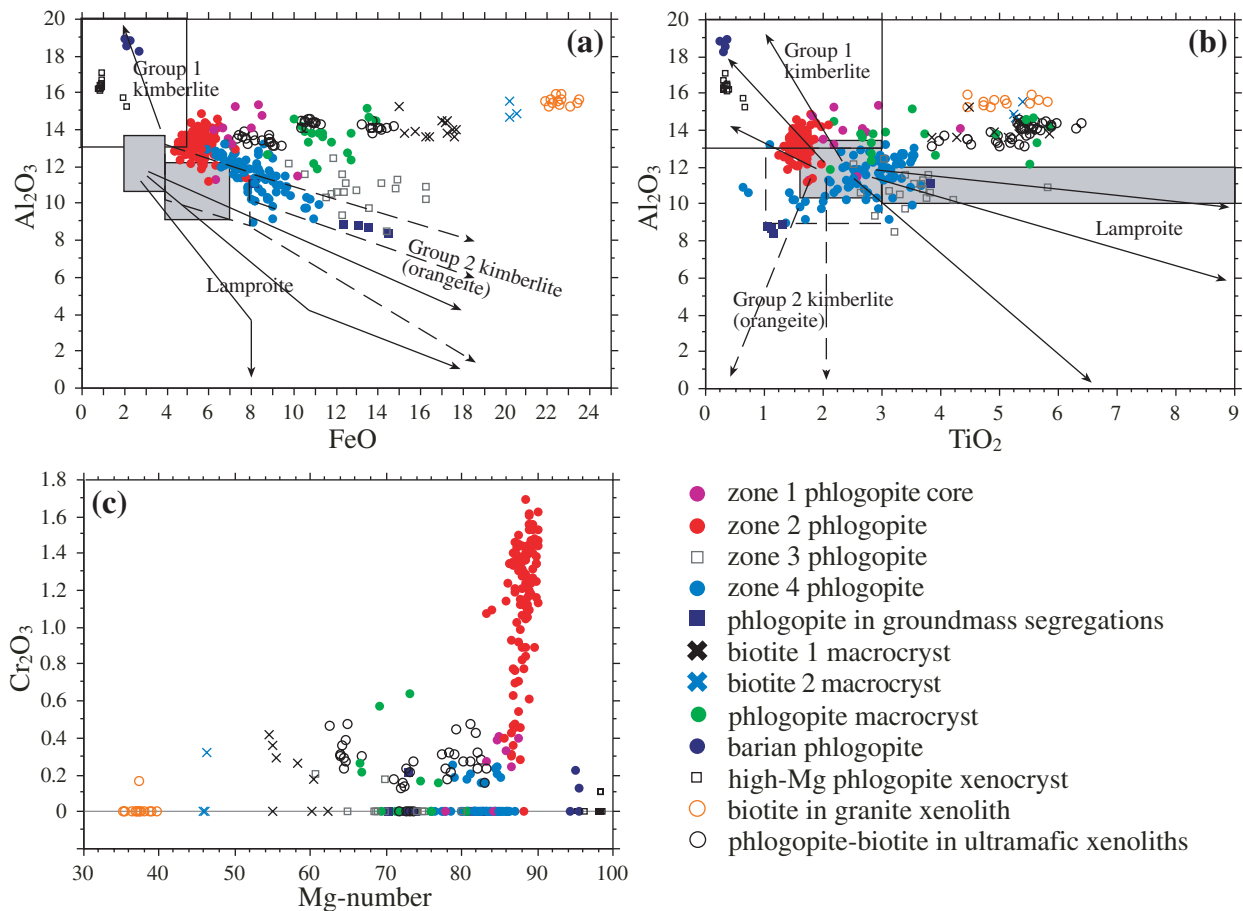
Fig. 5. Major-element variation diagrams for phlogopite–biotite from the Aries kimberlite and contained xenoliths. (a) Al_2O_3 (wt %) vs FeO (wt %); (b) Al_2O_3 (wt %) vs TiO_2 (wt %); (c) Cr_2O_3 (wt %) vs Mg-number. In (a) and (b), compositional fields for phenocrysts, and evolutionary trends in the composition of groundmass micas are indicated for lamproite (light-grey shaded fields, and labelled continuous lines), Group 2 kimberlites (orangeites; dashed box and lines), and Group 1 kimberlite (labelled box and continuous lines) (Mitchell, 1995).

Dark-brown phlogopite phenocryst cores (zone 1)

The cores of some phlogopite phenocrysts contain zones and patches of dark-brown phlogopite, up to 1 mm wide, with slightly higher Fe and Ti contents than the surrounding zone 2 composition phlogopite (Table 3; Figs 3j, 5a, b). The boundaries between these zones and the subsequent overgrowths of phlogopite can be highly irregular and may not be sharply defined by resorption surfaces. Phlogopite phenocrysts with zone 1 cores are rare, and have only been identified in samples of the MPK from the central and north lobes. The trace-element contents of zone 1 phlogopites generally plot quite close to those of zone 2 phlogopite phenocrysts (Fig. 6a–f). Zone 1 phlogopite from the central lobe (AN55-131·57m) is high in Sr (91–121 ppm), whereas zone 1 phlogopite from the north lobe (AN15-195·27m) is higher in Nb, but lower in Sr (35·5–37·3 ppm; Table 4; Fig. 6a, d). Both Co (71–82 ppm) and V (153–242 ppm) are slightly elevated in

zone 1 phlogopite cores in comparison with the zone 2 phlogopite phenocrysts (Table 4; Fig. 6e).

High-Cr phlogopite phenocrysts (zone 2)

A widespread population of phlogopite phenocrysts ($\leq$10% in volume; $\leq$1·5 mm long) is common to both the MPK and the OPRK phases. These phenocrysts are commonly euhedral, but some show evidence of resorption and rounding at the ends of laths and generally lack inclusions of other minerals (Fig. 3a–i). In regions of hypabyssal kimberlite with globular segregationary textures, these phlogopite phenocrysts lack phlogopite overgrowth rims. In terms of Al, Ti, Fe content, these phenocrysts are quite tightly constrained (Fig. 5a, b; $\sim$1·2–1·9 wt % TiO_2), and partially overlap with the compositions of phlogopite phenocrysts in both lamproites and Group 2 kimberlites (orangeites) as defined by Mitchell (1995). However, overall, the Aries phenocrysts are generally more aluminous. As a

Table 4: Representative LA-ICP-MS trace-element analyses of phlogopite-biotite from the Aries kimberlite and contained xenoliths. Major elements analysed by EDS.

Sample	AN55-131.57m	AN69-59.65m	AR51	AN29-234.15m	AN15-95.77m	AN15-195.27m	AN55-131.57m	AN15-195.27m	AN55-131.57m
Lobe	central	north ext	north	north	north	north	central	north	central
Analysis number	14A3	49B1	111A1	48A1	23A1	29A1	11A1	211A1	19B2
Position	core	core	core	core	core	core	core	core	core
Rock type	MPK	granite	xenolith	xenolith	SK	MPK	MPK	MPK	MPK
Mica type	Mg-phlog	bt in xen	phlog in xen	phlog in xen	phlog mac	z1 phlog	z1 phlog	z2 phlog	z2 phlog
SiO_2	39·39	34·83	39·25	37·62	37·39	39·88	36·18	38·77	38·83
TiO_2	0·68	5·81	5·19	5·33	2·79	2·59	4·13	1·46	1·58
Al_2O_3	15·30	15·59	13·29	14·59	13·46	11·51	14·52	13·61	12·98
Cr_2O_3	0·00	0·00	0·32	0·00	0·00	0·00	0·00	1·43	1·35
FeO	2·11	21·86	8·87	10·68	10·12	10·22	7·62	5·54	4·57
MnO	0·00	0·00	0·00	0·00	0·00	0·18	0·19	0·18	0
MgO	24·16	7·50	17·89	15·97	18·72	20·29	20·11	21·55	22·52
CaO	0·11	0·00	0·00	0·00	0·00	0·00	0·00	0	0
Na_2O	0·00	0·00	0·00	0·45	0·63	0·35	0·00	0	0
K_2O	10·40	9·59	10·15	9·79	9·07	9·22	9·41	9·65	10·19
Oxide total	92·15	95·18	94·96	94·43	92·18	94·24	92·16	92·19	92·02
Mg number	95·33	37·94	78·23	72·71	76·72	77·96	82·46	87·39	89·78
LA-ICP-MS									
(ppm) ^{47}Ti	4077	34831	31114	31953	16726	15527	24759	8753	9472
(ppm) Li	1·92	11·1	12·0	16·0	40·3	7·09	12·0	5·74	12·5
(wt%) CaO	0·038	0·017	0·059	0·024	0·048	0·039	0·073	0·041	0·037
(ppm) V	132	357	664	1112	225	153	216	100	79
Cr	318	264	1618	839	14·9	942	1327	7890	9594
Fe	15166	171592	72066	82466	88060	88667	56820	46533	38726
Co	10·8	67	115	106	94	79	74	61	62
Ni	39·7	43·6	534	126	125	195	306	786	907
^{66}Zn	54	385	81	96	70	64	48·2	39·3	37·6
^{68}Zn	46·9	224	96	149	160	101	206	86	94

Table 4: continued

Sample	AN55-131.57m	AN69-59.65m	AR51	AN29-234.15m	AN15-95.77m	AN15-195.27m	AN55-131.57m	AN15-195.27m	AN55-131.57m
Lobe	central	north ext	north	north	north	north	central	north	central
Analysis number	14A3	49B1	111A1	48A1	23A1	29A1	11A1	211A1	19B2
Position	core	core	core	core	core	core	core	core	core
Rock type	MPK	granite	xenolith	xenolith	SK	MPK	MPK	MPK	MPK
Mica type	Mg-phlog	bt in xen	phlog in xen	phlog in xen	phlog mac	z1 phlog	z1 phlog	z2 phlog	z2 phlog
Rb	191	743	328	156	357	426	428	599	683
Sr	22·7	1·95	1·56	2·33	76	37·3	118	45·7	33·1
Y	0·044	0·103	0·328	0·409	0·386	0·196	0·520	0·194	0·208
Zr	0·224	0·251	0·822	1·02	2·65	3·63	2·60	1·76	1·57
Nb	9·03	47·3	7·45	7·38	109	87	45·8	25·9	29·2
Cs	13·1	16·4	2·43	11·7	4·19	5·58	4·08	5·84	5·63
Ba	564	1542	2457	5012	6157	3380	7516	3312	2933
La	0·118	0·029	0·098	0·166	0·022	0·032	0·013	0·010	0·016
Ce	0·133	0·065	0·151	0·212	0·012	0·039	0·010	bdl	0·013
Nd	0·057	0·025	0·121	0·007	0·109	0·035	bdl	bdl	0·012
Sm	0·019	0·050	0·001	bdl	0·045	bdl	bdl	0·014	0·025
Eu	0·038	0·006	0·026	0·048	0·068	0·037	0·060	0·035	0·026
Gd	0·020	0·029	0·082	0·126	0·086	bdl	0·112	0·038	0·087
Dy	bdl	bdl	0·046	0·026	bdl	0·020	bdl	0·010	0·011
Er	bdl	0·012	0·071	0·005	bdl	0·001	bdl	bdl	0·013
Yb	bdl	bdl	0·061	0·026	0·010	bdl	bdl	0·039	bdl
Hf	0·028	0·094	0·058	0·065	0·139	0·156	0·168	0·116	0·059
Rb/Sr	8·4	381	211	67	4·7	11·4	3·6	13·1	20·6
Nb/Zr	40·3	189	9·1	7·3	41·0	23·9	17·6	14·7	18·6

Abbreviations: bdl, below detection limits; xen, xenolith; bt, biotite; phlog, phlogopite; mac, macrocryst; Mg-phlog, high-Mg phlogopite; z1/2, zone1/2; ext, extension
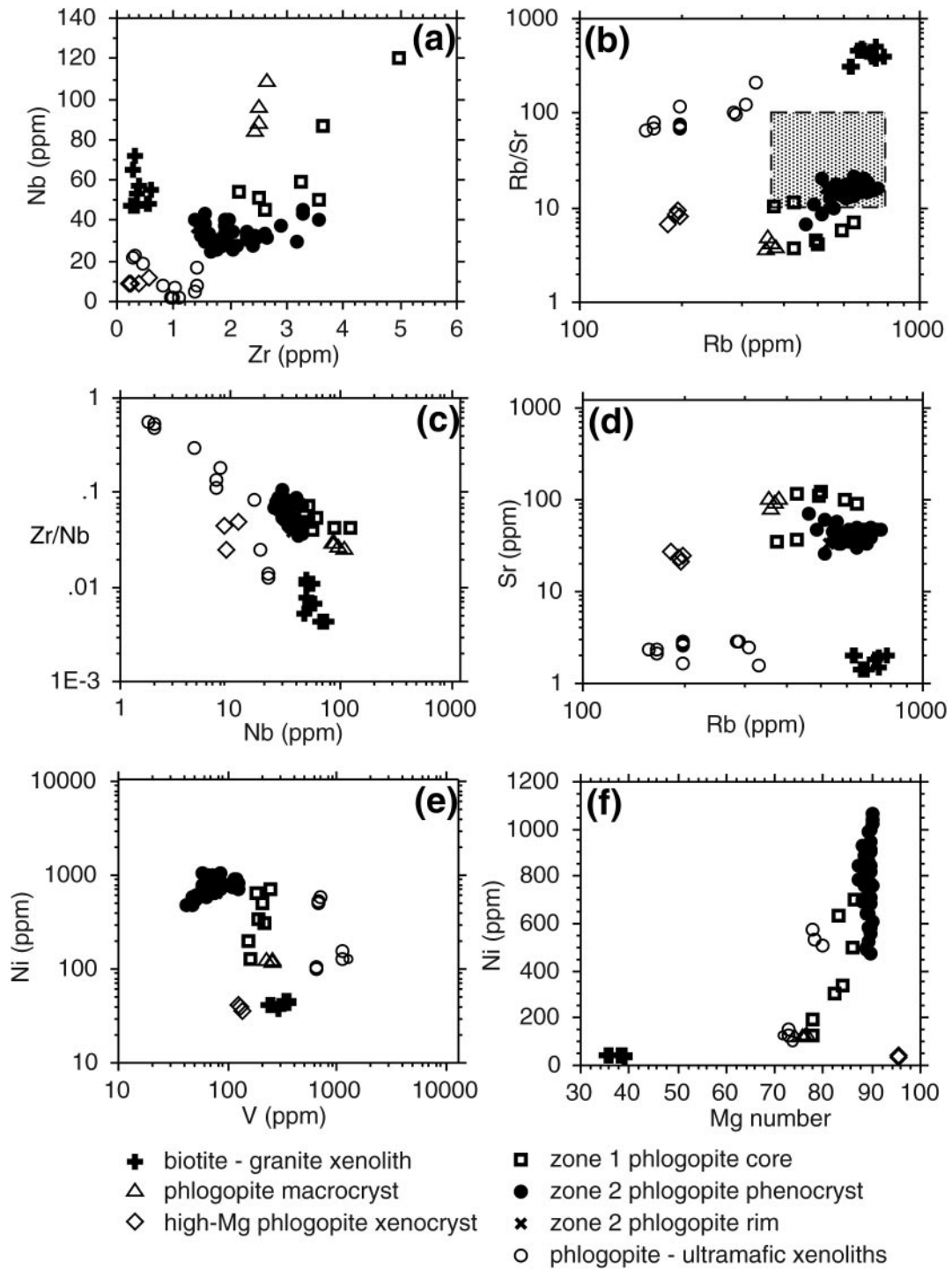
Fig. 6. Trace-element variation diagrams for phlogopite–biotite from the Aries kimberlite and contained xenoliths. The shaded box in Fig. 6b defines the field for phlogopite from metasomatized mantle xenoliths from South African kimberlites (Ionov *et al.*, 1997; Gregoire *et al.*, 2002).

population, the phenocrysts exhibit a distinctive trend of increasing Cr_2O_3 content, up to a maximum of 1·7 wt %, with increasing Mg-number from ∼83 to 90 (Fig. 5c).

Zone 2 phlogopite phenocrysts are tightly constrained in trace-element contents (Fig. 6a–f), including ∼50–70 ppm Co, and low V (<150 ppm). Their content of Ni varies over quite a large range (477–1061 ppm;

Fig. 6f) and shows an apparent correlation with Cr_2O_3 (Table 4).

High-Ti phlogopite–biotite in rims and groundmass (zone 3)

One of the generations of phlogopite overgrowth rims on earlier phenocrysts and macrocrysts is a dark-brown, high-Fe–Ti phlogopite–biotite. These rims are very thin ($\leq 5\,\mu m$) (Fig. 3b, d, f, g) and phlogopite–biotite of this composition also occurs in the groundmass of OPRK as a very fine-grained phase (Fig. 3d, g). This generation of phlogopite–biotite in rims and groundmass shows a limited compositional trend to lower Al_2O_3 with an increase in FeO in comparison with phlogopite phenocryst cores (Fig. 5a). This trend in groundmass and rim compositions correlates with the biotite trend observed by Mitchell (1995) in Group 2 kimberlites (orangeites), although the Aries phlogopites are more aluminous.

Groundmass phlogopite (zone 4)

A later stage of phlogopite growth occurs as overgrowths on phlogopite phenocrysts and macrocrysts, and as fine-grained masses to coarse-grained interlocking laths, <3 mm long, in the groundmass of MPK. These phlogopite rims commonly contain inclusions of groundmass chromite and magnetite. This stage of phlogopite growth also shows a limited trend to depletion in Al with increasing Fe content with respect to the composition of zone 2 phlogopite phenocrysts (Fig. 5a). However, none of the groundmass micas in the hypabyssal phases at Aries shows the strong Al depletion that is seen in groundmass micas from lamproites and Group 2 kimberlites (orangeites), which have a large tetra–ferriphlogopite component (Mitchell, 1995).

Barian aluminous phlogopite

Rare barian phlogopite occurs in an unusual groundmass segregation in one sample from the central lobe (AN55-131·57m; Fig. 4c). These grains contain 7·52–12·68 wt % BaO and 18·22–18·98 wt % Al_2O_3 (Table 3). The subhedral phlogopite grains are ≤ 0.5 mm long, and colourless in thin section. They occur in a concentrically zoned ~ 9 mm wide groundmass segregation that contains abundant calcite, with fewer numbers of disseminated pyrite grains, apatite (forming sprays of acicular crystals in calcite), magnetite and serpentine.

Phlogopite–biotite in ultramafic and granite xenoliths

The compositional ranges of micas in the three serpentinized ultramafic xenoliths are presented in Table 3. The phlogopite–biotites in the xenoliths are TiO_2-rich and show variations in Mg-number, but are relatively constant in Al_2O_3 content (Fig. 5a–c). The composition of high-Ti biotite from a granite xenolith (AN69-59·65m) from the north extension lobe is distinct from that of the high-Ti phlogopite–biotite contained in the other xenoliths, and any of the high-Ti phlogopite–biotite macrocrysts in the Aries kimberlite, being higher in Fe (Table 3; Fig. 5a–c).

High-Ti phlogopite grains from two of the serpentinized ultramafic xenoliths (AR51 and AN29-234·15m) have low Nb, Zr, Rb, and very low Sr contents, and high Co (86–121 ppm) and V (642–1289 ppm) concentrations (Table 4; Fig. 6a–e). Ni contents vary from 100–154 ppm in AN29-234·15m, to 509–574 ppm in AR51, and correlate with the Cr_2O_3 contents (Fig. 6e, f; Table 4). The high-Ti biotite from the granite xenolith also contains relatively low concentrations of Zr (0·251–0·608 ppm) (Fig. 6a) and very low Sr (1·40–2·04 ppm), but is high in Rb (621–786 ppm) (Fig. 6d). The very low Ni contents (37·2–46·3 ppm) also appear to correlate with the Cr_2O_3 contents (52–261 ppm Cr; Fig. 6e, f; Table 4). The most distinctive feature of the trace-element chemistry of the phlogopite–biotite from the xenoliths is the very low Sr contents that result in high Rb/Sr ratios of 308–496 for the granite xenolith, and 67–211 for the ultramafic xenoliths (Fig. 6b).

Amphiboles

The OPRK contains laths and fine-grained granular groundmass grains of potassian richterite (Na/K 4·2–5·7) containing 0·73–1·49 wt % TiO_2 and 1·32–2·32 wt % Al_2O_3 (including one grain of magnesiokatophorite with a Na/K ratio of 3·48, 1·35 wt % TiO_2, and 3·2 wt % Al_2O_3; Table 2; Fig. 7). The groundmass segregation amphiboles within the OPRK vary in composition from potassic richterite (Na/K ratio of 1·93–3·05, 0·33–0·86 wt % TiO_2, and 0·11–1·1 wt % Al_2O_3), to actinolite (at the rims of some crystals), and magnesio-arfvedsonite (Na/K ratio of 2·96–3·35, and 0·57–0·66 wt % TiO_2) (Table 2). The trends in amphibole composition follow a decrease in Al, Ti, Mg and Ca and an increase in K and Fe from groundmass potassian richterite to potassic richterite in the segregations. Within the segregations, the magnesio–arfvedsonite has higher contents of Na than the potassic richterite (Table 2), and some grains are zoned from potassic richterite cores to actinolite rims showing a decrease in Na and K, and a large increase in Ca from the core to rim, respectively.

WHOLE-ROCK GEOCHEMISTRY

The geochemistry of the main hypabyssal phase of the Aries kimberlite has been described in detail by
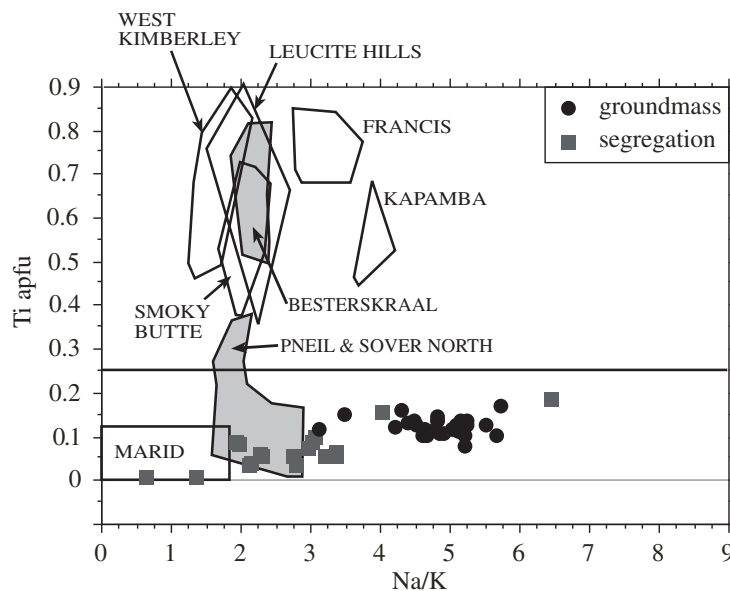
Fig. 7. Ti (apfu) vs Na/K for amphiboles from the Aries kimberlite. The fields for amphiboles from MARID xenoliths, lamproites and Group 2 kimberlites (orangeites; grey shaded fields) from Mitchell (1995) are shown. Dividing line at 0·25 apfu Ti is the lower limit for 'titanian' amphiboles.

Edwards *et al.* (1992) and Taylor *et al.* (1994) based on earlier drill-core material. In our study, we analysed eight new drill-core samples to determine the extent of geochemical variations that occur with the observed petrographic variations from MPK to the minor, differentiated OPRK and MSDU phases. Three of these analyses of MPK were rejected on the basis of (1) the contamination index (CI) of Clement (1982), and (2) examination of the CaO/Al_2O_3 ratios as an indicator of the degree of talc alteration. The compositions of two unaltered samples of MPK from the north lobe are similar to analyses reported by Edwards *et al.* (1992) and Taylor *et al.* (1994) (Table 5; Fig. 8a, b), the only differences being lower concentrations of Na_2O, Cr and Ni in the samples analysed in our study.

The MSDU dykes show a depletion in SiO_2, Al_2O_3, TiO_2 and K_2O, and an enrichment in Fe_2O_3 and MgO in comparison with MPK (Table 5). The depletion in K_2O is pronounced and reflects the very low phlogopite content of the MSDU dykes. Sr contents are relatively similar between MSDU and MPK (Fig. 8a), and Ni (1200 ppm) contents are higher in MSDU than in the MPK samples reported in this study (Table 5). Notably, the MSDU is higher in Pb, U and Th than MPK or OPRK (Fig. 8a; Table 5). The incompatible elements, Y, Zr, Nb and Ta, are relatively constant in the MPK and MSDU (Fig. 8a; Table 5). The contents of rare earth elements (REE) and the chondrite-normalized REE patterns of MPK and MSDU are also similar (Fig. 8a, b).

Two samples of OPRK from the north extension lobe show marked increases in SiO_2, Na_2O and, to a smaller extent, K_2O in comparison with the MPK. This is accompanied by a substantial decrease in MgO and Ni contents (Table 5). The OPRK is substantially enriched in Sr (1020–1180 ppm) and depleted in Ta and Th compared with the MPK and MSDU (Fig. 8a). These samples of OPRK are also depleted in light REE (LREE) relative to MPK and MSDU (Fig. 8b). Zr is moderately enriched, and Nb depleted, in comparison with the MPK and MSDU (Fig. 8a). Although the contamination indices for these OPRK samples were high (2·44–2·57; Table 5), we have reported them to provide an indication of the general geochemical variation from the MPK to the differentiated OPRK phase.

$^{40}AR/^{39}AR$ GEOCHRONOLOGY

Thirteen grains of mica, ranging in size from 188 to 1185 μm long, were selected for UV laser $^{40}Ar/^{39}Ar$ analysis from two kimberlite samples (AN65-36·82m OPRK; AN15-99·55m MPK), one granite xenolith (AN69-59·65m) and two serpentinized ultramafic xenoliths (AR51, AR61 from DDH AN29) from the north and north extension lobes. Cores and rims of grains were analysed by UV laser spot analysis and 15 mm wide line traverses were undertaken on the larger 476–974 mm diameter grains. One high-Ti phlogopite–biotite macrocryst from an OPRK sample (AN65-36·82m) retained an apparent $^{40}Ar*$ diffusive loss

Table 5: *Whole-rock major and trace-element analyses of hypabyssal lithologies from the Aries kimberlite*

Sample number	AN4-90·81m	AN5-168·12m	AN15-185·73m	AN65-36·82m	AN65-54·3m	AP 5/93·5	AP 2/67-76	Aries Av.	Ol lamp Av.	Micaceous kimb Av.
Rock type	MSDU	MPK	MPK	OPRK	OPRK	MPK	MPK			
(wt %) SiO_2	35·5	41·1	37·5	51·1	49·4	40·1	41·1	39·9	40	37
Al_2O_3	2·35	5	5·15	5·15	5·52	4·76	3·75	4·1	3·7	3·8
Fe_2O_3	15·98	10·73	12·2	11·06	11·52	10·94	11·07	9·3	7·9	8
TiO_2	0·81	1·08	1·36	0·97	1·06	1·35	1·07	1·1	3·2	1·4
Na_2O	0·09	0·06	0·05	2·11	1·77	0·63	0·69	0·6	0·4	0·2
K_2O	0·02	2·03	1·77	2·97	2·43	3·28	1·5	2·3	3·8	3·3
CaO	4·74	5·45	5·93	5·94	5·26	6·21	7·32	7·6	4·9	6·9
MgO	28·7	24·5	24·2	16·8	18·4	23·1	21·4	22·2	24	26·7
MnO	0·26	0·18	0·17	0·21	0·2	0·2	0·14	0·2	0·1	0·2
P_2O_5	0·66	0·41	0·52	0·4	0·4	0·26	0·29	0·3	1·3	1
LOI	10·13	8·78	10·37	2·7	3·37	8·11	10·39	-	-	-
Mg-number	65·9	71·1	68·1	62·1	63·3	69	68	72	76·6	78·3
CI	1·32	1·62	1·54	2·57	2·44	1·53	1·87			
K_2O/Na_2O	0·15	22·26	23·29	0·93	0·90	3·43	1·43	2·52	6·25	10·86
K_2O/Al_2O_3	0·01	0·44	0·37	0·62	0·48	0·75	0·43	0·61	1·11	0·94
$(K_2O + Na_2O)/Al_2O_3$	0·07	0·46	0·39	1·30	1·00	0·96	0·74	0·85	1·29	1·03
(ppm) F	n.d	n.d	n.d	3550	3250	1600	1800			
Sc	17	20·3	29·6	n.d	n.d	25	24			
V	83	116	148	125	134	88	85			
Cr	856	740	1030	1130	1240	2230	1982			
Co	n.d	n.d	n.d	85·9	75·6	n.d	n.d			
Ni	1200	787	655	524	480	1024	1559			
Cu	9	193	202	140	157	235	292			
Zn	153	91	131	111	76	114	141			
Ga	5·5	9·4	8·3	7	8	n.d	n.d			
Sn	n.d	n.d	n.d	3	2	n.d	n.d			
W	n.d	n.d	n.d	1	9	n.d	n.d			
Cs	n.d	n.d	n.d	1·5	2	n.d	n.d			
Rb	4·8	105	114	106	102	223	120			
Sr	598	535	373	1180	1020	542	314			
Y	11	11·3	13·5	11·9	13·6	15	16			
Zr	77	77	101	132	138	100	92			
Nb	367	387	442	324	343	472	400			
Ba	137	1410	1820	2150	1720	2332	1496			
La	280	351	298	228	227	268	234			
Ce	409	443	407	302	300	433	340			
Pr	40	39	37·3	24·2	24·9	n.d	n.d			
Nd	101	93·6	95·3	65·3	67·1	103	82			
Sm	10·2	9·6	10·7	7·4	7·3	9·94	8·59			
Eu	2·1	2·5	2·6	2	2	2·09	1·91			
Gd	n.d	n.d	n.d	6·5	6·6	n.d	n.d			
Tb	0·8	0·8	0·9	0·7	0·7	0·5	0·5			
Dy	2·8	2·8	3·2	2·8	3·1	n.d	n.d			
Ho	0·5	0·5	0·6	0·5	0·5	<1	<1			
Er	n.d	n.d	n.d	1·2	1·3	n.d	n.d			
Tm	0·1	0·1	0·2	0·2	0·2	n.d	n.d			

Table 5: continued

Sample number	AN4-90·81m	AN5-168·12m	AN15-185·73m	AN65-36·82m	AN65-54·3m	AP 5/93·5	AP 2/67-76	Aries Av.	Ol lamp Av.	Micaceous kimb Av.
Rock type	MSDU	MPK	MPK	OPRK	OPRK	MPK	MPK			
Yb	0·8	0·8	1·1	1	1·2	1·04	1·09			
Lu	0·1	0·1	0·2	0·2	0·2	0·15	0·16			
Hf	1·8	1·9	2·7	3	3	2·1	1·6			
Ta	27	25·4	29	16·5	17·4	30	25·6			
Pb	60	21	26	31	11	n.d	n.d			
Th	58·1	47·8	48·9	31	34	55·2	48·6			
U	9·3	5·2	6·5	3·9	4·3	3·6	4·2			

Comparative analyses from Edwards *et al.* (1992) and Taylor *et al.* (1994); CI (Contamination Index) = $(SiO_2 + Al_2O_3 + Na_2O)/(MgO + K_2O)$ (Clement, 1982); Mg-number = $100*Mg/(Mg + Fe^{2+})$ for Fe_2O_3/FeO (wt) = 0·2; n.d., not determined; ol, olivine; lamp, lamproite; Av., average; LOI, loss on ignition. Detection limits: AN4-90·81m, AN5-168·12m, AN15-185·73m-SiO_2, MgO (0·1); Al_2O_3-P_2O_5 (0·01); V-Zn, Sr, Zr, Ba, Pb (1); Sc, Ga, Hf (0·5); Rb, Nb, Ta (0·2); Y, La-Lu, U, Th (0·1). AN65-36·82m, AN65-54·3m-Na_2O, K_2O (0·05), P_2O_5 (0·1), SiO_2-MnO (0·01); F (40); Cr (10); V, Ni-Zn, Y, Pb (5); Ga-W, Nb, Hf, Th (1); Co, Zr, Ba-Ce, Nd, Ta, U (0·5); Rb (0·2); Cs, Sr, Pr, Sm-Lu (0·1).

profile with older ∼951–952 Ma core ages and younger rim ages (Fig. 9; Electronic Appendix 1, available at http://www.petrology.oxfordjournals.org/). Excluding four young 745–793 Ma $^{40}Ar/^{39}Ar$ ages from a total of 19 ages obtained from small mica grains or the rims of larger grains yielded a weighted mean $^{40}Ar/^{39}Ar$ age of 815·4 ± 4·3 Ma (95% confidence, $n = 15$), which is interpreted to be the kimberlite eruption age (Electronic Appendix 1).

The duration of kimberlite ascent for the north extension lobe was estimated via modelling of the core to rim $^{40}Ar*$ diffusive loss profiles obtained from one 590 μm diameter high-Ti phlogopite–biotite grain (see Analytical Methods section). This approach is identical to that of Pearson *et al.* (1997), Kelley & Wartho (2000), Kempton *et al.* (2001) and Wartho & Kelley (2003), although the grains used in our study were generally smaller than those used in previous studies.

The high-Ti phlogopite–biotite macrocryst from the OPRK sample AN65-36·82m exhibited a ∼10 μm thick overgrowth rim of phlogopite. This thin overgrowth was not thought to unduly modify the $^{40}Ar*$ diffusive loss profile in this 590 μm diameter grain. Because of the composition of the high-Ti phlogopite–biotite macrocryst in the OPRK sample AN65-36·82m (∼17 wt % FeO (Table 3)), it was difficult to assign a definite set of Ar diffusion parameters to this sample; therefore, the data were modelled using the Ar diffusion parameters for both Fe–biotite (Grove & Harrison, 1996) and phlogopite (Giletti, 1974). The $^{40}Ar/^{39}Ar$ data and the result of the modelling are shown in Fig. 9 and Electronic Appendix 1.

DISCUSSION
Classification: is Aries a kimberlite or a lamproite?

The classification of alkaline rocks is a difficult and often controversial process. Edwards *et al.* (1992) classified Aries as a micaceous kimberlite on the basis of its mineralogical, geochemical and isotopic characteristics, in agreement with the criteria recommended by Woolley *et al.* (1996). In light of the occurrence of a minor richterite- and sanidine-bearing hypabyssal phase (OPRK) in the north extension lobe of the Aries kimberlite—mineralogical characteristics that might suggest lamproitic affinities—it is worth re-examining the basis for its classification. In Table 6, the mineralogical characteristics of the Aries kimberlite are compared with those of olivine lamproites and Group 2 kimberlites (orangeites). At Aries, hypabyssal kimberlite (MPK and OPRK) contains phlogopite phenocrysts that are similar in chemistry to, but, as a group, are more aluminous than, 'primitive' phlogopite from lamproites and Group 2 kimberlites (orangeites; Fig. 5a, b, using fields defined by Mitchell, 1995). Phlogopite rims on macrocrysts and phenocrysts, and groundmass phlogopite show similar compositional trends to groundmass phlogopite in lamproites and Group 2 kimberlites (orangeite), but lack the strong Al depletion which is characteristic of a large tetra–ferriphlogopite component. Both MPK and OPRK contain high-Ti phlogopite–biotite macrocrysts with close textural and compositional similarities to those described from South African Group 2 kimberlites (orangeites) and other micaceous kimberlites worldwide
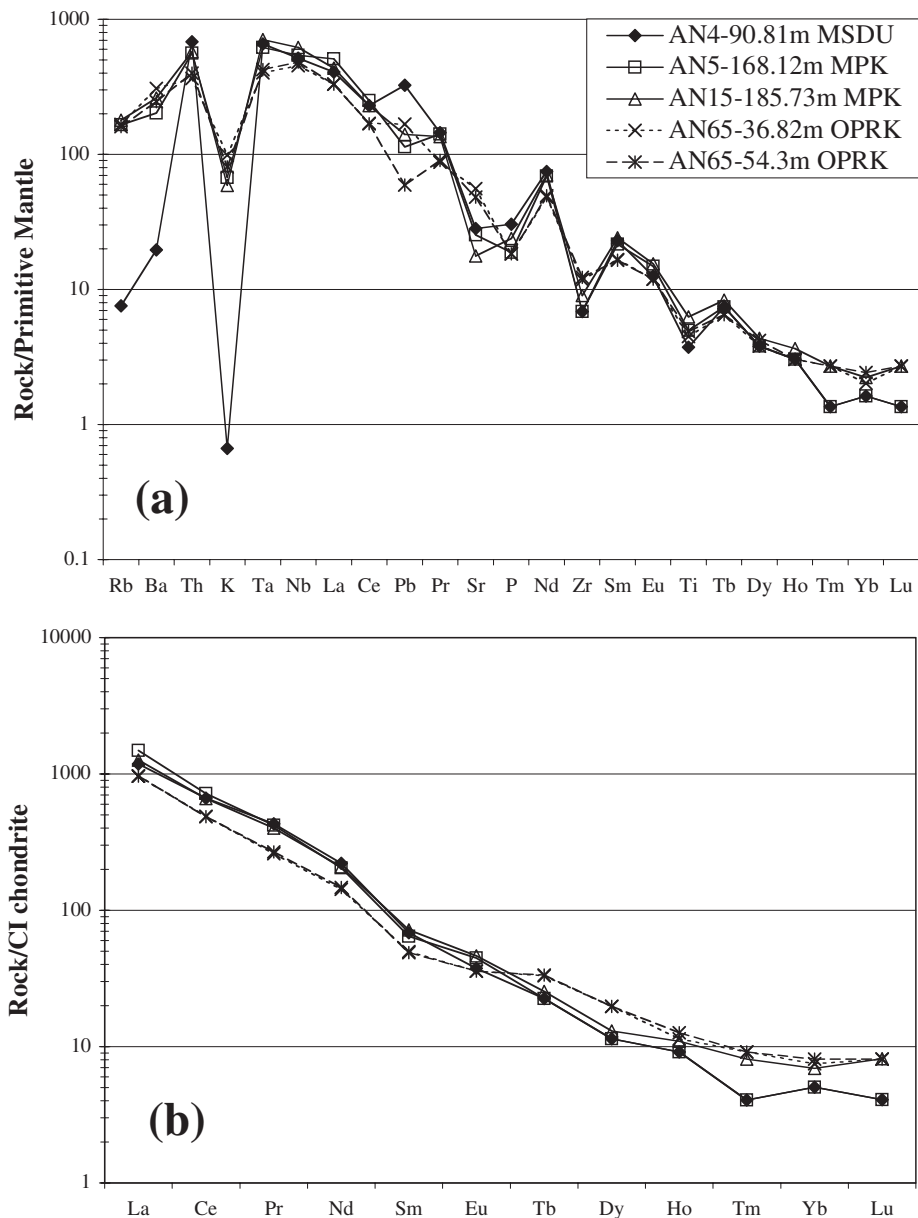
Fig. 8. (a) Primitive mantle-normalized trace-element abundance patterns, and (b) chondrite-normalized REE profiles for hypabyssal lithologies from the Aries kimberlite. All normalizing values are taken from Sun & McDonough (1989).

('type 1' mica of Smith *et al.*, 1978; Mitchell, 1995; Figs 5a, b, 10). Serpentine and calcite are common in the groundmass and groundmass segregations of MPK (Table 6).

The paragenesis of amphiboles in the Aries kimberlite (OPRK) is similar to that described for amphiboles in evolved varieties of Group 2 kimberlite (orangeite; Mitchell, 1995), where compositional variation also includes zonation from potassium richterite cores to magnesio–arfvedsonite rims (e.g. Pniel, South Africa).

Of these occurrences, the amphiboles in OPRK are most similar to those described from Pniel (low TiO$_2$), but generally have higher Na/K ratios in comparison (Mitchell, 1995; Fig. 7). Mitchell (1995) also noted the occurrence of Ti-poor magnesio–arfvedsonites as rims on richterite in lamproites. Mitchell & Bergman (1991) interpreted this rimming relationship in lamproites as being because of pre-existing amphiboles reacting with late-stage, Na- and Fe-rich deuteric fluids. It appears that amphiboles of similar composition occur in a range
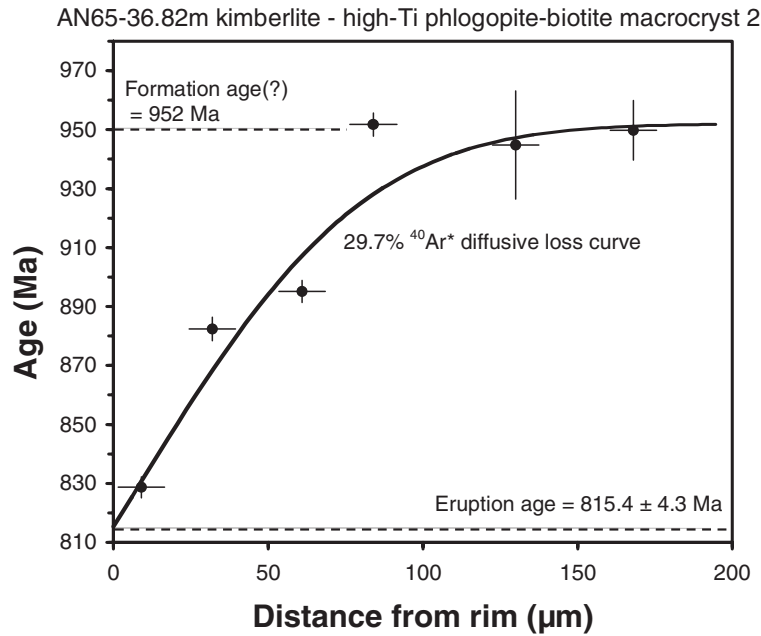
Fig. 9. A radiogenic ^{40}Ar diffusive loss profile from a high-Ti phlogopite–biotite macrocryst in the OPRK (AN65-36·82m) from the north extension lobe.
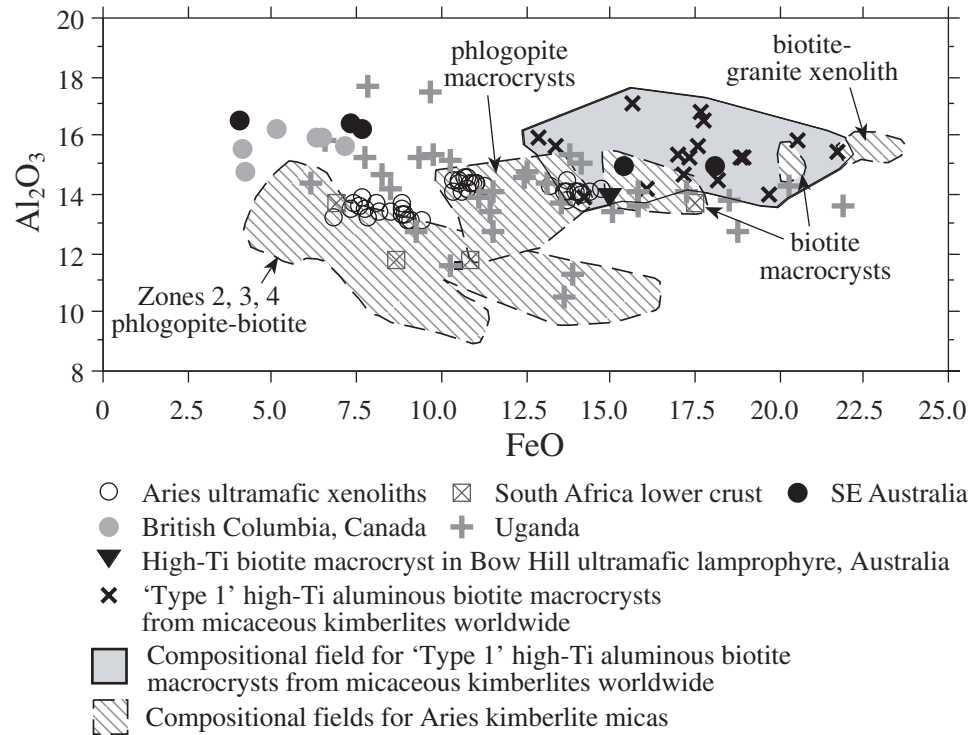
Fig. 10. Al$_2$O$_3$(wt %) vs FeO (wt %) for the Aries micas with comparative data for high-Ti phlogopite–biotite from spinel–facies mantle xenoliths worldwide. The compositional field for 'Type 1' high-Ti aluminous biotite macrocrysts from micaceous kimberlites worldwide also is shown (Lloyd & Bailey, 1975; Smith *et al.*, 1978; Griffin *et al.*, 1979, 1984; Wass, 1979; Canil & Scarfe, 1989; Fielding & Jaques, 1989; Lloyd *et al.*, 1991, 1999, 2002; Mitchell, 1995; Wiese *et al.*, 1996). Rock types: British Columbia—lherzolite, dunite, wehrlite; South Africa—lower crustal garnet granulite, garnet websterite; SE Australia—lherzolite, wehrlite, amphibole or apatite xenoliths; Uganda—pyroxenite, wehrlite.

Table 6: A comparison of the mineralogy of the Aries kimberlite (Edwards et al., *1992 and this study) with Group 2 kimberlites (orangeites) and lamproites (after Mitchell, 1996)*

	Aries	Group 2 kimberlites (orangeites)	Lamproites
Olivine			
-macrocrysts	Common to rare ($\leq$50%), may be resorbed	Common	Rare, primarily olivine lamproites
-phenocrysts	Common, twins and saw-tooth crystal groups in OPRK	Common	Common, resorbed/dog's tooth
Mica			
-macrocrysts	Minor biotite–phlogopite xenocrysts	Common	Rare
-phenocrysts	Common, phlogopite	Abundant, phlogopite	Common, Ti phlogopite, F-bearing
-groundmass	Abundant, lacks strong Al depletion and Fe^{3+}-rich phlogopite	Abundant, Ti-poor, Fe^{3+}-rich phlogopite	Common (Na)–Ti–Fe^{3+}-rich phlogopite, rare Ti biotite
Spinels	Rare to common, Mg chromite–Ti magnetite–magnetite	Rare, Mg chromite–Ti magnetite	Rare, Mg chromite–Ti magnetite
Diopside	Minor to common, $\leq$1·67 wt % TiO_2, $\leq$0·94 wt % Al_2O_3, $\leq$2·5 wt % Na_2O	Common, Al–Ti-poor	Common, Al–Ti-poor
Perovskite	Absent	Rare, Sr–REE-rich	Rare, Sr–REE-rich
Apatite	Common, $\leq$5·4 wt % SrO	Abundant, Sr–REE-rich	Common, Sr–REE-rich
Calcite	Common	Common	Absent
Leucite	Absent	Very rare	Common phenocrysts
Sanidine	Minor; in groundmass and segregations in OPRK, $\leq$3·56 wt % BaO, $\leq$1·71 wt % Fe_2O_3	Rare groundmass	Common phenocrysts and groundmass
K-Batitanates	Absent	Common	Common, V-poor, Cr-rich hollandites
Wadeite	Absent	Rare	Common
Shcherbakovite	Absent	Absent	Common
Richterite	Minor. Potassian richterite in groundmass, and potassic richterite, magnesio-arfvedsonite and actinolite in segregations in OPRK	Rare, K–Ti	Common, K–Ti
Ilmenite–pyrophanite	Rare, $\leq$32·6 wt % MnO	Common	Very rare

of alkaline rocks of distinct petrogenesis, and Mitchell & Bergman (1991) suggested that this may occur because of a convergence in amphibole evolutionary trends.

The most common groundmass Ti-bearing oxide phases at Aries are Nb-bearing rutile and aeschynite–(Ce). Aries lacks any of the groundmass titanates that are characteristic of lamproites (Table 6). The rare barian phlogopite that occurs in a groundmass segregation in one sample from the central lobe at Aries appears to be anomalous for the kimberlite as a whole, and is considered to have formed in a chemically unusual microenvironment (Table 3; Fig. 5a, b). Similarly, andradite is not widespread as a groundmass phase in MPK, and does not indicate that the kimberlite has affinities to ultramafic lamprophyres (Table 2).

On the basis of mineralogy alone, the Aries kimberlite probably would be classified as a Group 2 kimberlite (orangeite). However, as reported by Edwards *et al.* (1992) and Taylor *et al.* (1994), Aries has the Sr–Nd isotopic signature of a Group 1 kimberlite, and distinctive trace-element ratios (e.g. high Nb/Zr, low P/Ce) that distinguishes it from lamproites and Group 2 kimberlites (orangeites). Thus, Aries illustrates the mineralogical convergence that can occur between compositionally similar alkaline magmas of distinct petrogenesis. This again highlights the problem of over-reliance on mineralogical criteria in the classification of micaceous kimberlites with Group 1 isotopic signatures versus Group 2 kimberlites (orangeites) and lamproites, as discussed by Taylor & Kingdom

(1999) in relation to the Jagersfontein micaceous kimberlite.

Origin of high-Ti phlogopite–biotite macrocrysts

Smith *et al.* (1978) first identified minor aluminous biotite macrocrysts ('type 1' biotite) in micaceous kimberlites from South Africa (Swartruggens, Saltpeterpan, Monteleo) and Canada (Upper Canada Mine, Ontario) that were overgrown by later generations of phlogopite. Because of compositional similarities with some micas from carbonatites, Smith *et al.* (1978) suggested that these macrocrysts might have been derived from carbonatite magmas, via magma mixing. More detailed work by Mitchell & Meyer (1989) and Mitchell (1995) identified biotite macrocrysts of similar paragenesis from other South African Group 2 kimberlites (orangeites; New Elands, Sover Mine, Bellsbank). On the basis of the prominent association of these aluminous biotite macrocrysts with Group 2 kimberlites (orangeites) and a lack, in these rocks, of associated mantle xenoliths containing mica of similar composition, Mitchell & Meyer (1989) suggested that the biotites might not be xenocrysts derived from mantle or crustal rocks. Following this line of reasoning, Mitchell (1995) postulated that the aluminous biotites might have a 'genetic affinity with Group 2 kimberlite (orangeite) magmas or a relationship to their source regions'. Other micaceous kimberlites that contain aluminous biotite macrocrysts with a similar paragenesis include the Cross kimberlite, Canada (Hall *et al.*, 1989) and the Fayette County kimberlite, USA (Wiese *et al.*, 1996). In Western Australia, high-Ti biotite macrocrysts of this type occur in the Bow Hill UML in the east Kimberley (Fielding & Jaques, 1989).

The paragenetic sequence at Aries indicates that these aluminous high-Ti phlogopite–biotite macrocrysts were inherited early in the crystallization history of the magma, prior to the crystallization of the early phlogopite phenocryst population (zone 2), and subsequently were overgrown by up to three different generations of phlogopite (zones 2–4; Figs 3a–j, 5a–c). The high-Ti phlogopite–biotite macrocrysts commonly were resorbed prior to overgrowth by later generations of phlogopite, indicating disequilibrium with the kimberlite magma (Fig. 3c). Some possible sources for these macrocrysts include the mixing of early batches of magma, or inheritance from mantle or crustal lithologies during ascent. Our data show that some of the Aries high-Ti phlogopite–biotite macrocrysts overlap in major-element composition with the field of 'type 1' biotite macrocrysts recognized worldwide, but that the high-Ti phlogopite macrocrysts extend to higher Mg-numbers (Table 3; Figs 5a–c, 10). Serpentinized ultramafic xenoliths (AR51, AR61, AN29-234·15m) from the Aries kimberlite also contain high-Ti phlogopite–biotite grains that are chemically similar to some of the high-Ti phlogopite–biotite macrocrysts (Table 3, Figs. 5a–c). This association provides some evidence for their derivation from the disaggregation and assimilation of entrained xenoliths. However, trace-element data for phlogopite–biotite from a limited range of samples does not show an overlap between high-Ti phlogopite–biotite from xenoliths and macrocrysts from the Aries kimberlite (Figs. 6a–f). These data remain inconclusive, and a range of sources of phlogopite–biotite from within the lithospheric mantle and the crust may be involved that are not necessarily represented by the preserved Aries xenoliths.

The composition of the aluminous high-Ti phlogopite–biotite macrocrysts bears a broad resemblance to high-Ti phlogopite–biotite found in metasomatized spinel facies mantle lithologies, including, for example, xenoliths from Uganda (Lloyd & Bailey, 1975; Lloyd *et al.*, 1991, 1999, 2002) and SE Australia (Wass, 1979; Griffin *et al.*, 1984; Fig. 10). In these spinel facies xenolith suites, associated metasomatic minerals can include kaersutite–pargasite amphibole, diopside, ilmenite, magnetite, rutile, apatite and carbonates; the metasomatic fluids may have been basaltic or carbonatitic in nature (Menzies & Chazot, 1995; Ionov *et al.*, 1997). Some garnet facies xenolith suites may also preserve evidence of Fe–Ti-rich mantle metasomatism, such as those from the Matsoku kimberlite, Lesotho, which are characterized by the IRPS (Ilmenite, Rutile, Phlogopite, Sulphide, Spinel) mineral suite (Harte *et al.*, 1987), and those from the Proterozoic Premier kimberlite, South Africa (Danchin, 1979; Hoal, 2003). This Fe–Ti-rich style of metasomatism, involving silicate melts, is distinct from that of MARID (Mica, Amphibole, Rutile, Ilmenite, Diopside) suite (low-Ti phlogopite, K–richterite, rutile, ilmenite, diopside) and PIC (Phlogopite, Ilmenite, Clinopyroxene) suite xenoliths from Phanerozoic South African kimberlites (Menzies & Chazot, 1995; Gregoire *et al.*, 2002, 2003). The high-Ti phlogopite–biotite + rutile metasomatic association that occurs in serpentinized ultramafic xenoliths from the Aries kimberlite shows similarities to phlogopite–rutile associations in IRPS xenoliths described by Harte *et al.* (1987); however, the Aries xenolith micas are more TiO_2-rich by comparison, and the xenoliths lack garnet. Although the preserved evidence is sparse, the mineralogy of the metasomatized Aries xenoliths might indicate an Fe–Ti-rich geochemical signature for the metasomatism, similar to that occurring in spinel facies mantle and IRPS xenoliths.

The distinctively high Rb/Sr ratios and low Sr contents of phlogopite–biotite from the Aries granite and metasomatized ultramafic xenoliths, are similar to

those in some micas from metasomatized xenoliths from South African kimberlites (Fig. 6b, d; Table 4; Ionov *et al.*, 1997; Gregoire *et al.*, 2002). This trace-element signature might be distinctive of some metasomatic phlogopite in ancient lithospheric mantle, as the signature is not observed in phlogopite–biotite from fertile, non-cratonic metasomatized xenolith suites, where the Sr content of phlogopite may be buffered by co-existing metasomatic clinopyroxene (Ionov *et al.*, 1997). The low Nb and Zr contents of high-Ti phlogopite from the two serpentinized ultramafic xenoliths (AR51, AN29-234·15m; Fig. 6a) are similar to the Nb and Zr contents found in disseminated phlogopite in a range of metasomatized xenoliths from basalts, whereas the higher level of Nb in a phlogopite macrocryst from MPK (AN15-95·77m; Fig. 6a) falls within the range of Nb content in vein micas from these xenoliths (Ionov *et al.*, 1997).

In light of the evidence outlined above, we suggest that the occurrence of high-Ti phlogopite–biotite macrocrysts, that are similar in composition and paragenesis in the Aries kimberlite, the Bow Hill UML and other micaceous kimberlites in Canada and the USA, indicates that there may not be a special relationship between these micas and Group 2 kimberlite (orangeite) magmas. Rather, an origin involving inheritance through the disaggregation and assimilation of metasomatized spinel facies mantle xenoliths appears to be quite feasible.

Variations in mica chemistry with magma evolution

Chemical zonation of phlogopite phenocrysts and general variations in mica chemistry provide some insights into the magmatic evolution of the Aries kimberlite. The suite of mica xenocrysts or macrocrysts that occur in the various phases of the Aries kimberlite is quite diverse in composition (Table 3; Figs 5a–c, 10). Many of these micas may have been inherited through sampling of heterogeneous metasomatized mantle lithologies. The rare Mg–F-rich phlogopite xenocrysts that occur in MPK in the central and north lobes have a highly unusual composition (Tables 3, Tables 4; Figs 3i, 5a–c, 6a–f). If they are derived from the mantle, then their very high Mg-numbers possibly indicate crystallization from a carbonate-rich melt or an H_2O–CO_2 fluid interacting with highly refractory peridotite (cf. Ionov *et al.*, 1997). The patchy nature of zone 1 cores in phlogopite phenocrysts suggests that the mica was partially resorbed upon incorporation into the kimberlite magma. This phlogopite might represent an early mixing event prior to the crystallization of the zone 2 phlogopite phenocryst population, where zone 2 phlogopite overgrows zone 1 cores (Fig. 3j).

Populations of zone 2 phlogopite phenocrysts are common to both the MPK and OPRK phases of the kimberlite, suggesting that these two lithologies are related. Zone 2 phenocrysts are often euhedral and, less commonly, partially resorbed, which is indicative of mostly equilibrium crystallization from the magma (Fig. 3a–d, f, j). The high Cr_2O_3 contents in many of these phenocrysts suggest that they crystallized at mantle depths (Table 3; Fig. 5c; cf. Lloyd *et al.*, 2002). The zone 2 phlogopite phenocrysts are quite tightly constrained with respect to Al, Fe and Ti content, and the trend that they form of increasing Cr and Ni with increasing Mg-number, in the range ∼83–90 (Figs 5a–c, 6f), suggests that they crystallized from a magma that varied in Cr and Ni content. A possible source of this chemical variation may have been the entrainment and assimilation of mantle peridotite xenoliths, thus increasing the Mg-number, Cr and Ni content of the magma. A similar example of phlogopite xenocrysts exhibiting a range of Cr_2O_3 values from below detection limits to 1·16 wt % at Mg-numbers of 83–94 occurs in olivine melilitites from the Katwe–Kikorongo field in Uganda (Lloyd *et al.*, 2002), although these micas have higher TiO_2 contents (∼2–7 wt %) than those at Aries. Lloyd *et al.* (2002) attributed this chemical variation to the sampling of a heterogeneous mantle that introduced a mixture of wherlite and clinopyroxenite xenolithic micas, with variable Cr_2O_3 contents, into the magmas. In the Aries kimberlite, the generally euhedral morphology of the phlogopite phenocrysts and their tightly constrained compositions, with respect to Al, Ti and Fe (Fig. 5a, b), argues against an origin as xenocrysts derived from heterogeneous mantle lithologies, rather suggesting that they probably crystallized from the kimberlite magma.

At Aries, zone 3 phlogopite exhibits a compositional trend similar to the 'biotite trend' seen in phlogopite in Group 2 kimberlites (orangeites) as defined by Mitchell (1995; Fig. 5a). The occurrence of zone 3 phlogopite as very thin rims on phlogopite phenocrysts in MPK, and in the groundmass of OPRK, suggests that these phenocrysts interacted with evolving OPRK-type magma during ascent (Fig. 3b, d, f, g). Mitchell (1995) also noted that the 'biotite trend' in groundmass micas was more prevalent in evolved, more felsic phases of various Group 2 kimberlites (orangeites) from South Africa. At Aries, the occurrence in the groundmass of the more felsic OPRK suggests similar crystallization trends.

Although Edwards *et al.* (1992) suggested that there were differences in mica zonation between the lobes at Aries and between different lithologies, further sampling and more extensive analysis have produced a more coherent picture of mica chemical variation throughout the hypabyssal phases (Fig. 5a–c). Mica chemistry and

zonation suggests that, following the early inheritance of a range of chemically diverse phlogopite–biotite xenocrysts or macrocrysts, zone 2 phlogopite phenocrysts crystallized from a kimberlite magma that varied in Cr_2O_3 content—possibly controlled by the assimilation of mantle peridotite xenoliths—within the lithospheric mantle. These macrocrysts and phenocrysts were successively overgrown during ascent by zone 3 high-Fe–Ti phlogopite–biotite, in a differentiated OPRK-type magma, and zone 4 phlogopite rims. Zone 4 phlogopite rims on phlogopite phenocrysts are of the same chemical composition as fine-grained phlogopite that occurs in the adjacent groundmass of the host MPK. This suggests that zone 4 phlogopite rims crystallized immediately prior to the emplacement and cooling of the hypabyssal kimberlite dykes.

Origin of groundmass segregations and associated trends in the composition of groundmass minerals

Groundmass segregations are a common textural feature of Group 1 and 2 kimberlites, and Mitchell (1995) has suggested that they are produced by the separation into discrete areas of late-crystallizing components from the main part of the silicate–oxide groundmass in these rocks. In the Aries kimberlite, the composition of groundmass segregations varies from MPK, where groundmass segregations are dominated by phlogopite, serpentine, calcite and fluorapatite (Fig. 4a), to OPRK, where groundmass segregations are infilled with amphiboles, serpentine, sanidine and diopside (Fig. 4b). Thus, in each rock-type, the groundmass segregations are similar in composition to the enclosing, uniformly textured groundmass. In the OPRK, variations in mineral chemistry from the groundmass to segregations appear to reflect trends in the composition of residual fluids. This is most evident in the composition of amphiboles, where potassian richterite in the groundmass is higher in Al_2O_3 than amphiboles occurring in segregations. It is interesting to note that an Al-depletion trend is also observed in the composition of groundmass phlogopites (Fig. 5a). Potassic richterite occurring in the segregations has slightly higher K/Na ratios, although magnesio–arfvedsonites (commonly found rimming potassic richterite) are more sodic than richterite, reflecting a final stage of Na enrichment (Table 2). However, the amphibole chemistry is not uniform within the segregations, and this might reflect the influence of microenvironments within a heterogeneous groundmass. This effect is observed in the development of minor Ca-rich actinolite rims as opposed to magnesio–arfvedsonite in other groundmass segregations within the OPRK (Table 2). The groundmass segregations in the OPRK also appear to be richer in SiO_2, with the

crystallization of rare quartz that is absent from the surrounding groundmass (Fig. 4b). Overall, the Na-rich nature of the OPRK magma might have been the end result of differentiation involving the crystallization of phlogopite. Trends toward Na-rich, Al-poor, peralkaline residual liquids are common to several lamproites that have been studied, e.g. Gaussberg in Antarctica (Salvioli-Mariani et al., 2004), and these may provide an analogy for the petrogenesis of OPRK at Aries. Two samples of OPRK from the north extension lobe have whole-rock K/Na ratios of <1, which is quite different from samples of MPK (Table 5), and this might have had an influence on the crystallization of richterite in the OPRK (cf. Salvioli-Mariani et al., 2004).

Geochemical variation between hypabyssal phases

Some of the petrographic features of the MSDU dykes, particularly the occurrence of interstitial poikilitic diopside that occasionally encloses olivine macrocrysts, suggest that they formed as mafic cumulates from the main kimberlite magma. The genetic relationship between MSDU and MPK is shown by the close similarities in the REE signatures and overall trace-element geochemistry (Fig. 8a, b; Table 5). The elevated MgO and Ni contents of MSDU reflects the higher olivine content and high modal interstitial serpentine in this unit compared with the analysed samples of aphanitic MPK (Table 5). Sr contents remain constant between the MSDU and the MPK (Fig. 8a), suggesting a control by fluorapatite in the MSDU dykes. Notably, the MSDU has higher Pb, U and Th concentrations compared with MPK or OPRK (Fig. 8a; Table 5), and the presence of allanite–(Ce) in the MSDU probably controls the distribution of these elements. The strong K depletion in MSDU suggests the almost total separation of an Mg-rich magma from the main K-rich magma (Fig. 8a).

The occurrence of OPRK adjacent to the walls of the north extension lobe (Fig. 2) and its significant content of sandstone xenoliths, along with the high SiO_2 content and high contamination indices of the whole-rock samples (Table 5) suggest that the assimilation of country-rock sandstones played an important role in its petrogenesis. Some of the other geochemical features that could reflect assimilation include the relative depletion in LREE, MgO, Ni, Nb and Ta, probably because of dilution effects, and an enrichment in Zr possibly related to the entrainment of zircon from the sandstone (Table 5; Fig. 8a, b). OPRK contains a very low abundance of olivine macrocrysts, and the removal of olivine could have depleted the magma in MgO and Ni, in addition to any dilution effects from the assimilation of sandstone. The development of the

Na-rich OPRK magma probably also involved the protracted crystallization of phlogopite from MPK, where the crystallization of phlogopite with high K/Na ratios would increase the Na content of the residual magma. Although the whole-rock Al_2O_3 content of OPRK is similar to that of MPK (Table 5), its Al/Si ratio is greatly reduced, thereby allowing the crystallization of amphiboles and feldspars with lower Al/Si ratios (Table 2) than phlogopite. A trend of Al depletion is seen in the composition of phlogopite and amphiboles in the groundmass of OPRK (Fig. 5a), but is not reflected in the whole-rock composition (Table 5). An increase in a_{SiO2} in the residual fluids resulted in the crystallization of sanidine and rare quartz in the groundmass segregations (Fig. 4b).

$^{40}Ar/^{39}Ar$ geochronology

It has been shown in previous $^{40}Ar/^{39}Ar$ dating studies that phlogopites derived from mantle xenoliths commonly retain $^{40}Ar/^{39}Ar$ core ages that are older than the kimberlite eruption ages, and the phlogopite grain rims yield $^{40}Ar/^{39}Ar$ ages close to the kimberlite eruption ages (Phillips & Onstott, 1986; Phillips, 1991; Pearson *et al.*, 1997; Kelley & Wartho, 2000; Wartho & Kelley, 2003). This phenomenon was initially interpreted as being because of the presence of excess Ar, i.e. ^{40}Ar in excess of the $^{40}Ar*$ produced by the radioactive decay of ^{40}K (Lovering & Richards, 1964; Zartman *et al.*, 1967; Brookins, 1969; Kaneoka & Aoki, 1978; Fitch & Miller, 1983; Allsopp & Roddick, 1985; Phillips & Onstott, 1986, 1988). The presence of excess Ar in the mantle phlogopites was assigned to high Ar partial pressures preceding, or coinciding with, kimberlite eruption (e.g. Kaneoka & Aoki, 1978; Fitch & Miller, 1983; Phillips, 1991). However, several studies refute this earlier assumption, and have shown that mantle and lower crustal-derived phlogopites retain $^{40}Ar/^{39}Ar$ core ages that are geologically valid and in agreement with known geological event ages, including mantle metasomatic events, determined by other radiometric techniques (Pearson *et al.*, 1997; Kelley & Wartho, 2000; Kempton *et al.*, 2001; Wartho & Kelley, 2003). The retention of the older core ages is despite the fact that phlogopite does not retain Ar for geological periods above its maximum closure temperature of ~480°C (Giletti, 1974). A possible reason for this phenomenon is that a lack of fluid under mantle conditions would inhibit long-distance transport of Ar, which would thus partition preferentially into phlogopite (Kelley & Wartho, 2000; Wartho & Kelley, 2003). Therefore, $^{40}Ar*$ produced by ^{40}K decay in mantle phlogopites may be retained in the lattice for geological periods and retain meaningful $^{40}Ar/^{39}Ar$ ages (Kelley & Wartho, 2000; Wartho & Kelley, 2003). This closed system or partially closed system phenomenon has also been documented in other studies (e.g. Foland, 1979; Scaillet, 1996; Kühn *et al.*, 2000; Baxter *et al.*, 2002; Sherlock & Kelley, 2002).

One high-Ti phlogopite–biotite macrocryst from the OPRK sample AN65-36·82m retained a maximum $^{40}Ar/^{39}Ar$ core age of 952 Ma, and exhibited a short $^{40}Ar*$ diffusive loss profile, having lost 29·7% of its original $^{40}Ar*$ (Fig. 9; Electronic Appendix 1). As previously discussed, the ~10 μm phlogopite rim overgrowing the high-Ti phlogopite–biotite macrocryst made no discernable difference to the overall $^{40}Ar*$ loss profile in this 590 μm diameter grain. The 15 μm wide laser line raster at the rim of this grain yielded a $^{40}Ar/^{39}Ar$ age of $828·7 \pm 7·2$ Ma (2σ), which will be a mixed age, with components from both the ~10 μm wide phlogopite overgrowth and high-Ti phlogopite–biotite macrocryst. The other analysed micas all preserve evidence of extensive $^{40}Ar*$ loss, the majority having lost ~99% of their original $^{40}Ar*$ (Electronic Appendix 1).

The $^{40}Ar/^{39}Ar$ 952 Ma core age does not appear to correspond with any known mantle metasomatic, or geological events in the Kimberley region. Graham *et al.* (1999) produced isotopic evidence for multiple mantle events beneath the Kimberley Craton including; a ~1750–2000 Ma event corresponding to a period of possible NW-directed Palaeoproterozoic subduction beneath the Kimberley Craton; a ~1500 Ma event corresponding to the age of eclogite facies diamond growth at Argyle; and a ~1200 Ma event corresponding to the age of emplacement of the Argyle lamproite. SHRIMP U–Pb ages of zircons derived from one granite xenolith (1851 ± 10 Ma; Downes *et al.*, in preparation) and two serpentinized ultramafic xenoliths (1845 ± 30 and 1861 ± 31 Ma; Downes *et al.*, in preparation) correspond to the age of the Whitewater Volcanics and the Paperbark Supersuite of the Bow River Batholith in the Hooper and Lamboo Complexes (Griffin *et al.*, 2000). However, $^{40}Ar/^{39}Ar$ core ages of 984 ± 360 and 1016 ± 33 Ma were obtained from phlogopite grains from the Pteropus 02 kimberlite in the northern Kimberley, ~310 km to the NNW of the Aries kimberlite (Phillips, 1994).

One Aries mica grain retains old 951–952 Ma $^{40}Ar/^{39}Ar$ core ages and younger rim ages, which is indicative of $^{40}Ar*$ diffusive loss (Fig. 9). This $^{40}Ar*$ diffusive loss profile is formed because of the interaction of the mica grain with hot kimberlite magma during transport to the surface (Pearson *et al.*, 1997; Kelley & Wartho, 2000; Kempton *et al.*, 2001; Wartho & Kelley, 2003). $^{40}Ar*$ diffusive loss profiles can provide information on the duration of outgassing (i.e. ascent durations) for magmas; however, in order to do this, a magma temperature must be estimated. Although kimberlite magma temperatures could be in excess of ~1300°C at

their depth of origin in garnet–diamond facies mantle, experimental studies on a Group 2 kimberlite (orangeite) magma composition, similar to the Aries kimberlite, showed that the typical olivine + phlogopite + clinopyroxene phenocryst assemblage crystallized below 2·5 GPa ($\sim\leq$75 km depth) and $\leq$1200°C (Ulmer & Sweeney, 2002). This depth approximately corresponds to the spinel facies lithospheric mantle, within which we infer the high-Ti phlogopite–biotite macrocrysts within the Aries kimberlite to have been derived, and the zone 2 phlogopite phenocrysts to have crystallized. Fedortchouk & Canil (2004) calculated crystallization temperatures of Group 1 kimberlite magmas from Lac de Gras, Canada, of 1030–1170 ± 50°C (with a mean of $\sim$1080°C), at an assumed pressure of 1·0 GPa. This pressure would correspond to quite shallow depths within the crust. Later crystallization of the kimberlite groundmass may have occurred at $\sim$600°C (Stasiuk et al., 1999; Fedortchouk & Canil, 2004). For the sake of clarity, we will refer to a mean temperature of 1000°C (Electronic Appendix 1). Using this mean magma temperature, we calculated a kimberlite magma ascent duration for the north extension lobe of $\sim$0·23–2·32 days. This estimate probably only measures the duration of magma ascent from the spinel facies mantle ($\sim$35–75 km) to the surface, and provides no constraints on the initial rise from the diamond–garnet facies mantle ($\sim$>150 km) to the spinel facies. Unfortunately, no mica grains from the north lobe of the Aries kimberlite retained [40]Ar* diffusive loss profiles that were suitable for modelling. Although the $\sim$0·23–2·32 day estimate for the ascent of magma in the north extension lobe is quite rapid, and compares well with estimates for the ascent duration of various diamondiferous southern African kimberlites (0·9–6·9 days; Wartho & Kelley, 2003), the north extension lobe is poorly diamondiferous, and factors such as the nature of the mantle sampled by the magma probably were a greater influence on diamond grade in this case (Ramsay et al., 1994).

CONCLUSIONS

Taylor et al. (1994) suggested that the Aries kimberlite originated in diamond facies mantle through a small degree of partial melting of a fluorphlogopite-bearing (at <7 GPa) or a fluoro–K–richterite-bearing garnet peridotite (at >7 GPa). This theory is supported by the geochemical characteristics of the Aries kimberlite (Edwards et al., 1992; Taylor et al., 1994) and the nature of the mantle-derived xenocryst suite (Ramsay et al., 1994). The mantle source region may have been heterogeneous in composition, consisting of depleted peridotite, K–richterite-bearing metasomatized peridotite, and asthenospheric mantle components (Taylor et al., 1994). Following the generation of the Aries

kimberlite magma, its ascent to the surface may have occurred in stages, involving an initial rise from the diamond–garnet facies mantle, before interaction with, and sampling of, the spinel facies mantle (Edwards et al., 1992; Ramsay et al., 1994). This history is preserved via the chemistry of spinel and high-Ti phlogopite–biotite macrocrysts, serpentinized spinel-bearing ultramafic xenoliths and rare serpentinized phlogopite–biotite–rutile-bearing ultramafic xenoliths. Phlogopite–biotite chemistry and textural relationships indicate that the crystallization of phlogopite phenocrysts (zone 2 composition) in the kimberlite magma probably commenced within the spinel facies lithospheric mantle, following the inheritance of widespread, but minor, high-Ti phlogopite–biotite macrocrysts, some of which are similar to the 'type 1' micas of Smith et al. (1978). The compositional variation in these phenocrysts, i.e. to high Cr_2O_3 concentrations with increasing Mg-number, may have been produced by variations in magma chemistry because of the entrainment and assimilation of mantle peridotite. A possible early magma mixing event is also recorded in the higher Fe–Ti cores of some phlogopite phenocrysts in the central and north lobes (zone 1 phlogopite).

[40]Ar/[39]Ar geochronology yields a kimberlite eruption age of 815·4 ± 4·3 Ma (95% confidence). There is also evidence that rare high-Ti phlogopite–biotite macrocrysts retain evidence for a $\sim$950 Ma mantle metasomatic, or other resetting event. This metasomatic or resetting event would have been unrelated to the kimberlite volcanism as the two events are separated by 135 Ma. According to [40]Ar* diffusion modelling, the ascent of the kimberlite magma from the lithospheric mantle to its emplacement in the north extension lobe occurred over $\sim$0·23–2·32 days. This estimate probably only measures the duration of magma ascent from the spinel facies mantle ($\sim$35–75 km) to the surface, and provides no constraints on an initial rise from the diamond–garnet facies ($\sim$>150 km) to the spinel facies mantle.

The compositional and petrographic variation within the hypabyssal phases of the Aries kimberlite (MPK, OPRK and MSDU) suggests that low-pressure fractionation of the magma occurred in the near-surface environment. A Na–Si-rich residual phase (OPRK) developed near the margins of the north extension lobe. This OPRK magma probably evolved from MPK as a residual liquid following extended phlogopite crystallization, and was contaminated by the assimilation of sandstone country rock. Similarities in the compositions of phlogopite phenocryst populations in MPK and OPRK (zone 2 phlogopite) indicate that the two rocks are related. Rare MSDU dykes, that are K-poor, higher in MgO and lower in SiO_2 than MPK, may have developed as mafic cumulates from the main kimberlite magma (MPK).

ACKNOWLEDGEMENTS

SUPPLEMENTARY DATA

Supplementary data for this paper are available on *Journal of Petrology* online.

REFERENCES

Allsopp, H. L. & Roddick, J. C. (1985). Rb–Sr and ^{40}Ar–^{39}Ar age determinations on phlogopite micas from the pre–Lebombo Group Dokolwayo kimberlite pipe. *Special Publication of the Geological Society of South Africa* **13**, 267–271.

Baxter, E. F., DePaulo, D. J. & Renne, P. R. (2002). Spatially correlated anomalous $^{40}Ar/^{39}Ar$ age variations in biotites about a lithologic contact near Simplon Pass, Switzerland: A mechanistic explanation for excess Ar. *Geochimica et Cosmochimica Acta* **66**, 1067–1083.

Brookins, G. D. (1969). The significance of K–Ar dates on altered kimberlitic phlogopite from Riley County, Kansas. *Journal of Geology* **77**, 102–107.

Canil, D. & Scarfe, C. M. (1989). Origin of phlogopite in mantle xenoliths from Kostal Lake, Wells Gray Park, British Columbia. *Journal of Petrology* **30**, 1159–1179.

Canil, D. & Fedortchouk, Y. (1999). Garnet dissolution and the emplacement of kimberlites. *Earth and Planetary Science Letters* **167**, 227–237.

Clement, C. R. (1982). A comparative geological study of some major kimberlite pipes in the northern Cape and Orange Free State. Ph.D. thesis. University of Cape Town, South Africa, 432 pp.

Danchin, R. V. (1979). Mineral and bulk chemistry of garnet lherzolite and garnet harzburgite xenoliths from the Premier Mine, South Africa. In: Boyd, F. R. & Meyer, H. O. A. (eds) *The Mantle Sample: Inclusions in Kimberlites and Other Volcanics. Proceedings of the Second International Kimberlite Conference, Volume 2*. Washington, DC: American Geophysical Union, 104–126.

Edwards, D. (1990). The petrology and mineralogy of the Aries diamond pipe, Kimberley Block, Western Australia. Honours thesis. University of Western Australia, 58 pp.

Edwards, D., Rock, N. M. S., Taylor, W. R., Griffin, B. J. & Ramsay, R. R. (1992). Mineralogy and petrology of the Aries diamondiferous kimberlite pipe, central Kimberley Block, Western Australia. *Journal of Petrology* **33**, 1157–1191.

Eggins, S. M., Rudnick, R. L. & McDonough, W. F. (1998). The composition of peridotites and their minerals, a laser-ablation ICPMS study. *Earth and Planetary Science Letters* **154**, 53–71.

Fedortchouk, Y. & Canil, D. (2004). Intensive variables in kimberlite magmas, Lac de Gras. Canada and implications for diamond survival. *Journal of Petrology* **45**(9), 1725–1745.

Fielding, D. C. & Jaques, A. L. (1989). Geology, petrology and geochemistry of the Bow Hill lamprophyre dykes, Western Australia. In: Ross, J. *et al.* (eds) *Kimberlites and Related Rocks, Volume 1. Proceedings of the Fourth International Kimberlite Conference. Geological Society of Australia Special Publication* **14**, 206–219.

Fitch, F. J. & Miller, J. A. (1983). K–Ar age of the East Peripheral kimberlite at De Beers Mine, Kimberley, R. S. A. *Geological Magazine* **120**, 505–512.

Foland, K. A. (1979). Limited mobility of argon in a metamorphic terrain. *Geochimica et Cosmochimica Acta* **43**, 793–801.

Franz, L., Brey, G. P. & Okrusch, M. (1996). Reequilibration of ultramafic xenoliths from Namibia by metasomatic processes at the mantle boundary. *Journal of Geology* **104**, 599–615.

Giletti, B. J. (1974). Studies in diffusion I: Argon in phlogopite mica. In: Hofmann, A. W., Giletti, B. J., Yoder, H. S. & Yund, R. A. (eds) *Geochemical Transport and Kinetics. Washington: Carnegie Institute* **634**, 107–115.

Gorter, J. D. & Glikson, A. Y. (2002). Fohn lamproite and a possible Late Eocene–pre-Miocene diatreme field, Northern Bonaparte Basin, Timor Sea. *Australian Journal of Earth Sciences* **49**(5), 847–868.

Graham, S., Lambert, D. D., Shee, S. R., Smith, C. B. & Reeves, S. (1999). Re–Os isotopic evidence for Archaean lithospheric mantle beneath the Kimberley block, Western Australia. *Geology* **27**(5), 431–434.

Gregoire, M., Bell, D. R. & Le Roex, A. P. (2002). Trace element geochemistry of phlogopite-rich mafic mantle xenoliths: their classification and their relationship to phlogopite-bearing peridotites and kimberlites revisited. *Contributions to Mineralogy and Petrology* **142**, 603–625.

Gregoire, M., Bell, D. R. & Le Roex, A. P. (2003). Garnet lherzolites from the Kaapvaal Craton (South Africa): Trace element evidence for a metasomatic history. *Journal of Petrology* **44**(4), 629–657.

Griffin, T. J., Tyler, I. M. & Playford, P. E. (1993). Lennard River, WA (3rd edn). *Western Australia Geological Survey, 1:250 000 Geological Series Explanatory Notes*, 56 pp.

Griffin, T. J., Page, R. W., Sheppard, S. & Tyler, I. M. (2000). Tectonic implications of Palaeoproterozoic post-collisional, high-K felsic igneous rocks from the Kimberley region of northwestern Australia. *Precambrian Research* **101**, 1–23.

Griffin, W. L., Carswell, D. A. & Nixon, P. H. (1979). Lower-crustal granulites and eclogites from Lesotho, Southern Africa. In: Boyd, F. R. & Meyer, H. O. A. (eds) *The Mantle Sample: Inclusions in Kimberlites and Other Volcanics. Proceedings of the Second International Kimberlite Conference, Volume 2*. Washington, DC: American Geophysical Union, 59–86.

Griffin, W. L., Wass, S. Y. & Hollis, J. D. (1984). Ultramafic xenoliths from Bullenmerri and Gnotuk Maars, Victoria, Australia: Petrology of a sub-continental crust–mantle transition. *Journal of Petrology* **25**(1), 53–87.

Grove, M. & Harrison, T. M. (1996). $^{40}Ar*$ diffusion in Fe-rich biotite. *American Mineralogist* **81**, 940–951.

Gunn, P. J. & Meixner, A. J. (1998). The nature of the basement of the Kimberley Block, Northwestern Australia. *Exploration Geophysics* **29**, 506–511.

Hall, D. C., Helmstaedt, H. & Schulze, D. J. (1989). The Cross diatreme, British Columbia, Canada: A kimberlite in a young orogenic belt. In: Ross, J. (eds) *Kimberlites and Related Rocks, Volume 1. Proceedings of the Fourth International Kimberlite Conference. Geological Society of Australia Special Publication* **14**, 97–108.

Hames, W. E. & Bowring, S. A. (1994). An empirical evaluation of the argon diffusion geometry in muscovite. *Earth and Planetary Science Letters* **124**, 161–169.

Harte, B., Winterburn, P. A. & Gurney, J. J. (1987). Metasomatic and enrichment phenomena in garnet peridotite facies mantle xenoliths from the Matsoku kimberlite pipe, Lesotho. In: Menzies, M. A. & Hawkesworth, C. J. (eds) *Mantle Metasomatism*. London: Academic Press, 145–220.

Hoal, K. O. (2003). Samples of Proterozoic iron-enriched mantle from the Premier kimberlite. *Lithos* **71**, 259–272.

Hunter, R. H., Kissling, R. D. & Taylor, L. A. (1984). Mid- to late-stage kimberlitic melt evolution: phlogopites and oxides from the Fayette County kimberlite, Pennsylvania. *American Mineralogist* **69**, 30–40.

Ionov, D., Griffin, W. L. & O'Reilly, S. Y. (1997). Volatile-bearing minerals and lithophile trace elements in the upper mantle. *Chemical Geology* **141**, 153–184.

Jaques, A. L., Lewis, J. D. & Smith, C. B. (1986). *Kimberlites and Lamproites of Western Australia*. Geological Survey of Western Australia, Bulletin **132**. Perth, Western Australia. 268 pp.

Kaneoka, I. & Aoki, K. (1978). $^{40}Ar/^{39}Ar$ analysis of phlogopite nodules and phlogopite-bearing peridotites in South African kimberlites. *Earth and Planetary Science Letters* **40**, 119–129.

Kelley, S. P. & Wartho, J.-A. (2000). Rapid kimberlite ascent and the significance of Ar–Ar ages in xenolith phlogopites. *Science* **289**, 609–611.

Kempton, P. D., Downes, H., Neymark, L. A., Wartho, J.-A., Zartman, R. E. & Sharkov, E. V. (2001). Garnet granulite xenoliths from the northern Baltic Shield: the underplated lower crust of a Paleoproterozoic Large Igneous Province? *Journal of Petrology* **42**, 731–763.

Kühn, A., Glodny, J., Iden, K. & Austrheim, H. (2000). Retention of precambrian Rb/Sr phlogopite ages through Caledonian eclogite facies metamorphism, Bergen Arc Complex, W-Norway. *Lithos* **51**, 305–330.

Lloyd, F. E. & Bailey, D. K. (1975). Light element metasomatism of the continental mantle: the evidence and the consequences. *Physics and Chemistry of the Earth* **9**, 389–416.

Lloyd, F. E., Huntingdon, A. T., Davies, G. R. & Nixon, P. H. (1991). Phanerozoic volcanism of SW Uganda: a case for regional K and LILE enrichment beneath a domed rifted continental plate. In: Kampunzu, A. B. & Lubala, R. T. (eds) *Magmatism in Extensional Structural Settings*. Berlin: Springer-Verlag, 23–72.

Lloyd, F. E., Woolley, A. R., Stoppa, F. & Eby, G. N. (1999). Rift Valley magmatism: is there evidence for laterally variable alkali clinopyroxenite mantle? *Geolines* **9**, 76–83.

Lloyd, F. E., Woolley, A. R., Stoppa, F. & Eby, G. N. (2002). Phlogopite–biotite parageneses from the K–mafic–carbonatite effusive magmatic association of Katwe–Kikorongo, SW Uganda. *Mineralogy and Petrology* **74**, 299–322.

Lovering, J. F. & Richards, J. R. (1964). Potassium–argon age study of possible lower-crust and upper-mantle inclusions in deep-seated intrusions. *Journal of Geophysical Research* **69**, 4895–4901.

Menzies, M. & Chazot, G. (1995). Fluid processes in diamond to spinel facies shallow mantle. *Journal of Geodynamics* **20**(4), 387–415.

Mitchell, R. H. (1995). *Kimberlites, Orangeites and Related Rocks*. New York: Plenum Press, 410 pp.

Mitchell, R. H. (1996). The Orangeite Clan. In: Mitchell, R. H. (ed) *Undersaturated Alkaline Rocks: Mineralogy, Petrogenesis, and Economic Potential. Mineralogical Association of Canada, Short Course Volume 24*. Winnipeg, Manitoba, 245–257.

Mitchell, R. H. & Meyer, H. O. A. (1989). Mineralogy of micaceous kimberlites from the New Elands and Star Mines, Orange Free State, South Africa. In: Ross, J. *et al.* (eds) *Kimberlites and Related Rocks, Volume 1. Proceedings of the Fourth International Kimberlite Conference. Geological Society of Australia Special Publication* **14**, 83–96.

Mitchell, R. H. & Bergman, S. (1991). *Petrogenesis of Lamproites*. New York: Plenum Press, 447 pp.

Myers, J. S., Shaw, R. D. & Tyler, I. M. (1996). Tectonic evolution of Proterozoic Australia. *Tectonics* **15**, 1431–1446.

Nakagawa, M., Wada, K. & Wood, C. P. (2002). Mixed magmas, mush chambers and eruption triggers: evidence from zoned clinopyroxene phenocrysts in andesitic scoria from the 1995 eruptions of Ruapehu volcano, New Zealand. *Journal of Petrology* **43**, 2279–2303.

Neal, C. R. & Taylor, L. A. (1989). The petrography and composition of phlogopite micas from the Blue Ball kimberlite, Arkansas: a record of chemical evolution during crystallization. *Mineralogy and Petrology* **40**, 207–224.

O'Brien, H. E., Irving, A. J. & McCallum, I. S. (1988). Complex zoning and resorption of phenocrysts in mixed potassic mafic magmas of the Highwood Mountains, Montana. *American Mineralogist* **73**, 1007–1024.

Pearce, T. H., Russell, J. K. & Wolfson, I. (1987). Laser-interference and Nomarski interference imaging of zoning profiles in plagioclase phenocrysts from the May 18, 1980, eruption of Mount St Helens, Washington. *American Mineralogist* **72**, 1131–1143.

Pearson, D. G., Kelley, S. P., Pokhilenko, N. P. & Boyd, F. R. (1997). Laser $^{40}Ar/^{39}Ar$ analyses of phlogopites from Southern African and Siberian kimberlites and their xenoliths: constraints on eruption ages, melt degassing and mantle volatile compositions. *Russian Journal of Geology and Geophysics* **38**, 106–117.

Phillips, D. (1991). Argon isotope and halogen chemistry of phlogopite from South African kimberlites: a combined step-heating, laser probe, electron microprobe and TEM study. *Chemical Geology (Isotope Geosciences Section)* **87**, 71–98.

Phillips, D. (1994). *Confidential Internal Report to Stockdale Prospecting Ltd.* (KR94/034).

Phillips, D. & Onstott, T. C. (1986). Application of $^{36}Ar/^{40}Ar$ versus $^{39}Ar/^{40}Ar$ correlation diagrams to the $^{40}Ar/^{39}Ar$ spectra of phlogopites from Southern African kimberlites. *Geophysical Research Letters* **13**, 689–692.

Phillips, D. & Onstott, T. C. (1988). Argon isotopic zoning in mantle phlogopite. *Geology* **16**, 542–546.

Pidgeon, R. T., Smith, C. B. & Fanning, C. M. (1989). Kimberlite and lamproite emplacement ages in Western Australia. In: Ross, J. *et al.* (eds) *Kimberlites and Related Rocks, Volume 1. Proceedings of the Fourth International Kimberlite Conference. Geological Society of Australia Special Publication* **14**, 369–381.

Ramsay, R. R., Edwards, D., Taylor, W. R., Rock, N. M. S. & Griffin, B. J. (1994). Compositions of garnet and spinel from the Aries diamondiferous kimberlite pipe, central Kimberley Block, Western Australia: implications for exploration. *Journal of Geochemical Exploration* **51**, 59–78.

Rex, D. C. & Guise, P. G. (1995). Evaluation of argon standards with special emphasis on time scale measurements. In: Odin, G. S. (eds) *Phanerozoic Time Scale. Bull. Liais. Inform. IUGS Subcom. Geochronol*, **13**, 21–23.

Roberts, H. G. & Perry, W. J. (1969). *Mt Elizabeth, WA. 1:250 1969 000 Geological Series. Bureau of Mineral Resources, Australia, Explanatory Notes*, SE/52–5, 16 pp.

Salvioli-Mariani, E., Toscani, L. & Bersani, D. (2004). Magmatic evolution of the Gaussberg lamproite (Antarctica): volatile content and glass composition. *Mineralogical Magazine* **68**(1), 83–100.

Scaillet, S. (1996). Excess ^{40}Ar transport scale and mechanism in high-pressure phentites: a case study from an eclogitized metabasite of the

Dora–Maira nappe, western Alps. *Geochimica et Cosmochimica Acta* **50**, 1075–1090.

Sheppard, S., Griffin, T. J., Tyler, I. M. & Page, R. W. (2001). High- and low-K granites and adakites at a Palaeoproterozoic plate boundary in northwestern Australia. *Journal of the Geological Society, London* **158**, 547–560.

Sherlock, S. & Kelley, S. (2002). Excess argon evolution in HP–LT rocks: a UVLAMP study of phengite and K-free minerals, NW Turkey. *Chemical Geology* **182**, 619–636.

Singer, B. S., Pearce, T. H., Kolisnik, A. M. & Myers, D. (1993). Plagioclase zoning in mid-Pleistocene lavas from the Seguam volcanic center, central Aleutian arc, Alaska. *American Mineralogist* **78**, 143–157.

Singer, B. S., Dungan, M. A. & Layne, G. D. (1995). Textures and Sr, Ba, Mg, Fe, K, and Ti compositional profiles in volcanic plagioclase: clues to the dynamics of calc–alkaline magma chambers. *American Mineralogist* **80**, 776–798.

Smith, C. B. (1989). Rb–Sr mica age for sample ME/KIB 1145. *Triad Minerals N.L./Poseiden Pty Ltd Confidential Internal Report.*

Smith, J. V., Brennesholtz, R. & Dawson, J. B. (1978). Chemistry of micas from kimberlites and xenoliths: I. Micaceous kimberlites. *Geochimica et Cosmochimica Acta* **42**, 959–971.

Stasiuk, L. D., Lockhart, G. D., Nassichuk, W. W. & Carlson, J. A. (1999). Thermal maturity evaluation of dispersed organic matter inclusions from kimberlite pipes, Lac de Gras, Northwest Territories, Canada. *International Journal of Coal Geology* **40**, 1–25.

Steiger, R. J. & Jäger, E. (1977). Subcommission on geochronology: convention on the use of decay constants in geo- and cosmochronology. *Earth and Planetary Science Letters* **36**, 359–362.

Sun, S.-S. & McDonough, W. F. (1989). Chemical and isotopic systematics of oceanic basalts: implications for mantle composition and processes. In: Saunders, A. D. & Norry, M. J. (eds) *Magmatism in Ocean Basins. Geological Society Special Publication* **42**, 313–345.

Taylor, W. R. & Kingdom, L. (1999). Mineralogy of the Jagersfontein kimberlite—an unusual group 1 micaceous kimberlite—and a comment on the robustness of the mineralogical definition of 'orangeite'. In: Gurney, J. J., Gurney, J. L., Pascoe, M. D. & Richardson, S. H. (eds) *The P. H. Nixon Volume, Proceedings of the Seventh International Kimberlite Conference.* Capetown, South Africa: Red Roof Design, 861–866.

Taylor, W. R., Tompkins, L. A. & Haggerty, S. E. (1994). Comparative geochemistry of West African kimberlites: evidence for a micaceous kimberlite endmember of sublithospheric origin. *Geochimica et Cosmochimica Acta* **58**(19), 4017–4037.

Toscani, L., Contini, S. & Ferrarini, M. (1995). Lamproitic rocks from Cabezo Negro de Zeneta: brown micas as a record of magma mixing. *Mineralogy and Petrology* **55**, 281–292.

Towie, N. J., Marx, M., Bush, M., Manning, E. R. & Ramsay, R. R. (1994). The Aries diamondiferous kimberlite pipe, central Kimberley Region, Western Australia: exploration, setting and evaluation. In: Meyer, H. O. A. & Leonardos, O. H. (eds) *Proceedings of the Fifth International Kimberlite Conference, Araxa, June 1991. Volume 2: Diamonds: Characterization, Genesis and Exploration. CPRM Special Publication* **1B**, 319–328.

Tyler, I. M., Page, R. W. & Griffin, T. J. (1999). Depositional age and provenance of the Marboo Formation from SHRIMP U–Pb zircon geochronology: implications for the early Palaeoproterozoic tectonic evolution of the Kimberley region, Western Australia. *Precambrian Research* **95**, 225–243.

Ulmer, P. & Sweeney, R. J. (2002). Generation and differentiation of group II kimberlites: constraints from a high-pressure experimental study to 10 GPa. *Geochimica et Cosmochimica Acta* **66**(12), 2139–2153.

Wartho, J.-A. & Kelley, S. P. (2003). $^{40}Ar/^{39}Ar$ ages in mantle xenolith phlogopites: determining the ages of multiple lithospheric mantle events and diatreme ascent rates in southern Africa and Malaita, Solomon Islands. In: Vance, D., Müller, W. & Villa, I. M. (eds) *Geochronology: Linking the Isotope Record with Petrology and Textures. Geological Society of London, Special Publication* **220**, 231–248.

Wass, S. Y. (1979). Fractional crystallization in the mantle of late-stage kimberlitic liquids: evidence in xenoliths from the Kiama area, NSW, Australia. In: Boyd, F. R. & Meyer, H. O. A. (eds) *The Mantle Sample: Inclusions in Kimberlites and Other Volcanics. Proceedings of the Second International Kimberlite Conference, Volume 2.* Washington, DC: American Geophysical Union, 366–373.

Wiese, R. G., Edgar, A. D. & Barnett, R. L. (1996). Textural and compositional variations in phlogopite and biotite in kimberlite from Fayette County, Pennsylvania: a documentation of possible evolution of kimberlite magma. *Neues Jahrbuch fur Mineralogie Abh* **170**(2), 111–126.

Woolley, A. R., Bergman, S. C., Edgar, A. D., Le Bas, M. J., Mitchell, R. H., Rock, N. M. S. & Scott Smith, B. H. (1996). Classification of lamprophyres, lamproites, kimberlites, and the kalsilitic, melilitic, and leucitic rocks. *The Canadian Mineralogist* **34**, 175–186.

Zartman, R. E., Brock, M. R., Heyl, A. V. & Thomas, H. H. (1967). K–Ar and Rb–Sr ages of some alkalic intrusive rocks from central and eastern United States. *American Journal of Science* **265**, 848–870.